Cell

Force-Induced Bidirectional Stepping of Cytoplasmic Dynein

Arne Gennerich,[1] Andrew P. Carter,[1] Samara L. Reck-Peterson,[1] and Ronald D. Vale[1,*]
[1]The Howard Hughes Medical Institute and the Department of Cellular and Molecular Pharmacology, University of California San Francisco, San Francisco, CA 94158-2200, USA
*Correspondence: vale@cmp.ucsf.edu
DOI 10.1016/j.cell.2007.10.016

SUMMARY

Cytoplasmic dynein is a minus-end-directed microtubule motor whose mechanism of movement remains poorly understood. Here, we use optical tweezers to examine the force-dependent stepping behavior of yeast cytoplasmic dynein. We find that dynein primarily advances in 8 nm increments but takes other sized steps (4–24 nm) as well. An opposing force induces more frequent backward stepping by dynein, and the motor walks backward toward the microtubule plus end at loads above its stall force of 7 pN. Remarkably, in the absence of ATP, dynein steps processively along microtubules under an external load, with less force required for minus-end- than for plus-end-directed movement. This nucleotide-independent walking reveals that force alone can drive repetitive microtubule detachment-attachment cycles of dynein's motor domains. These results suggest a model for how dynein's two motor domains coordinate their activities during normal processive motility and provide new clues for understanding dynein-based motility in living cells.

INTRODUCTION

Cytoplasmic dynein is a two-headed molecular motor found in eukaryotic cells that uses the energy from ATP binding and hydrolysis to move toward the minus ends of microtubules. Cytoplasmic dynein, which is involved in a variety of motile processes such as mitotic spindle formation and the directed transport of organelles and mRNA (Vallee et al., 2004), is composed of two identical ~500 kDa heavy chains and several associated chains (Vale, 2003; Höök and Vallee, 2006). The heavy chain contains 6 AAA+ domains (AAA: *A*TPase *a*ssociated with diverse cellular *a*ctivities) arranged in a ring (Ogura and Wilkinson, 2001; Asai and Koonce, 2001) (Figure 1A). The first four AAA+ modules (AAA1–AAA4) have conserved nucleotide-binding and hydrolysis motifs. AAA domain 1 is essential for dynein motility, while the other sites (particular AAA3) may contribute important regulatory functions (Silvanovich et al., 2003; Reck-Peterson and Vale, 2004; Takahashi et al., 2004; Kon et al., 2004, 2005).

The microtubule-binding and putative mechanical domains of dynein are distinctly different from those of kinesin and myosin. A small, globular microtubule-binding domain (MTBD) is poised at the tip of an ~10–15 nm long "stalk" (Asai and Koonce, 2001; Burgess et al., 2003) (Figure 1A), which is an antiparallel coiled-coil that lies between the fourth and fifth AAA domains (Gee et al., 1997; Koonce and Tikhonenko, 2000). A second appendage emerging from the ring is an ~10 nm long "linker" element that lies predominantly on top of the ring (Figure 1A), although it has been observed in a detached state (Burgess et al., 2003). The linker's position shifts relative to the AAA+ ring in different nucleotide states (Burgess et al., 2003; Kon et al., 2005), and this conformational change has been suggested to produce force and unidirectional motion. N-terminal to the linker is a dimerization domain that joins the two motor domains, although its structure and mechanism of dimerization are not known. The dimerization domain then extends into a "tail" region that binds several dynein-associated chains, which are involved in cargo binding (Vallee et al., 2004).

Recent single-molecule motility assays with purified mammalian dynein (Wang et al., 1995; King and Schroer, 2000; Mallik et al., 2004, 2005; Toba et al., 2006; Ross et al., 2006) and recombinant cytoplasmic dynein from yeast (Reck-Peterson et al., 2006) have begun to shed light on dynein's molecular mechanism. All of these studies have concluded that a single dimeric cytoplasmic dynein molecule can move processively along microtubules. However, the details of the stepping mechanism have been more controversial. Mallik et al. (2004) first reported that brain cytoplasmic dynein takes predominantly 24–32 nm steps along microtubules under no load but decreases its step size to 8 nm near its stall force of ~1 pN. In contrast, a more recent optical trapping study with brain dynein reports that cytoplasmic dynein takes load-invariant steps of 8 nm and stalls at 6–8 pN (Toba et al., 2006). Using single-molecule fluorescence microscopy, Reck-Peterson et al. (2006) observed predominantly 8 nm steps but also a wide range of larger (12–24 nm) steps and backward steps as well. Differing from the studies above, Ross et al. (2006) reported that dynein, in the presence of dynactin, can undergo long (>1000 nm) movements

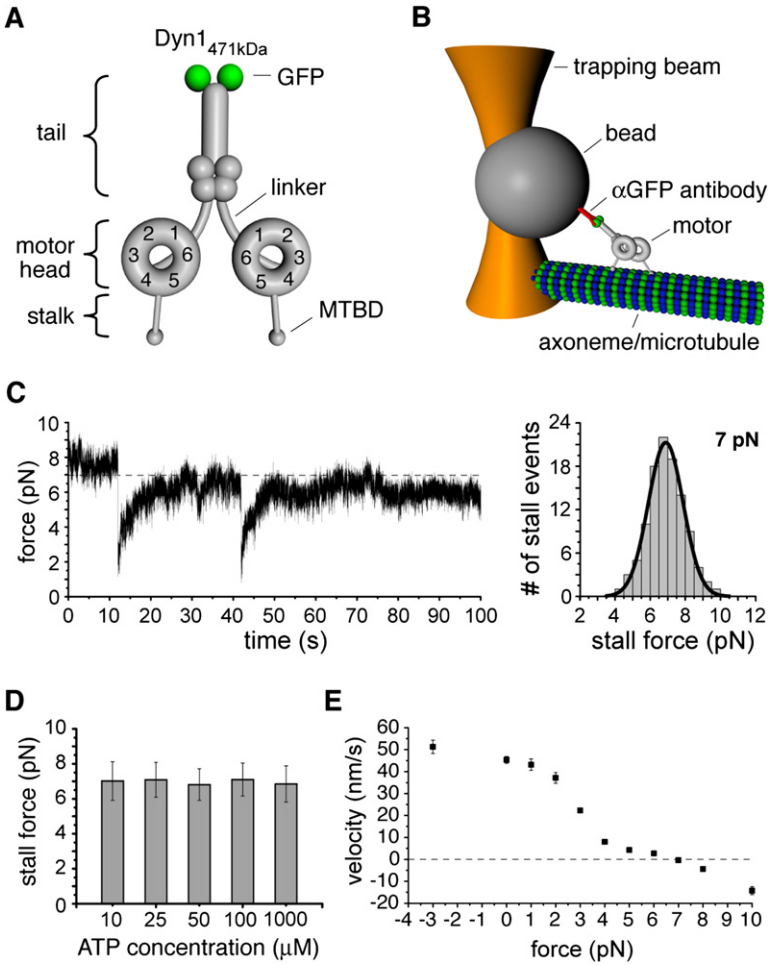

Figure 1. Force Production by Full-Length Dynein

(A) Illustration of the dynein dimer with associated chains and N-terminal GFPs.

(B) Schematic representation of the optical trapping assay (not to scale).

(C) Displacement of a single dynein molecule at 1 mM ATP in a fixed (nonfeedback) optical trap showing successive motor detachments and stalling events (trap stiffness: k = 0.055 pN/nm).The inset on the right side shows the stall force distribution (6.9 pN ± 1 pN; mean ± SD; n = 108).

(D) Stall force as a function of ATP concentration. Values are displayed as mean ± SD (n = 20–108).

(E) Velocity-force relationship at 1 mM ATP. All velocities were measured with the optical trap maintaining a constant load using feedback control, except the zero load velocity, which was measured by tracking the GFP-tagged motors in a single-molecule fluorescence assay. Values are displayed as mean ± SEM (n = 35–151).

toward the plus as well as the minus ends of microtubules. Thus, the mechanism of cytoplasmic dynein stepping and force production remains controversial.

In order to dissect the dynein mechanism, we used a force-feedback optical trap to analyze the stepping behavior of native and artificially dimerized yeast cytoplasmic dynein as a function of load. At low loads (1 pN), we show that dynein primarily advances by 8 nm as well as occasionally larger (12–24 nm) increments. Increasing loads (3–6 pN) frequently induce large (12–24 nm) alternating forward-backward displacements that fail to advance the motor and might be caused by a force-induced conformational change in the positioning of the two motor domains in the dynein dimer. Strikingly, we also find that dynein will walk processively toward either the minus or plus ends of microtubules under an applied force in the absence of nucleotide hydrolysis, a behavior that distinguishes dynein from kinesin-1 and myosin-V. A small assisting force (−3 pN) causes dynein to step toward the microtubule minus end (its normal direction) in the absence of nucleotide, while a much larger force (7–10 pN) is required to induce dynein stepping toward the plus end. The directional asymmetry of this force-induced, nucleotide-independent stepping suggests a model for how dynein's two motor domains are coordinated during normal processive motility and provides new clues for how dynein might respond to antagonistic forces in living cells.

RESULTS

Stall Force of Full-Length Yeast Cytoplasmic Dynein and Reversed Motion at Superstall Loads

Our previous study (Reck-Peterson et al., 2006) showed that *S. cerevisiae* full-length cytoplasmic dynein ($Dyn1_{471kDa}$, herein referred to as "dynein"), a complex of the dimerized motor-containing heavy chain and several associated chains, is a highly processive motor. Here we coupled dynein to anti-GFP antibody-coated 1 μm latex beads through an N-terminal GFP-tag on the motor tail (Figures 1A and 1B); the dynein density on the beads was adjusted so that there was a >99% probability that bead movements were due to single dynein molecules (Supplemental Data and Figure S1). Dynein-coated beads captured in a fixed position optical trap (nonfeedback mode) moved along sea urchin axonemes away from the trap center until they eventually stalled at an average rearward load of ~7 pN (Figure 1C), similar to the stall force of kinesin-1 (Visscher et al., 1999). Remarkably,

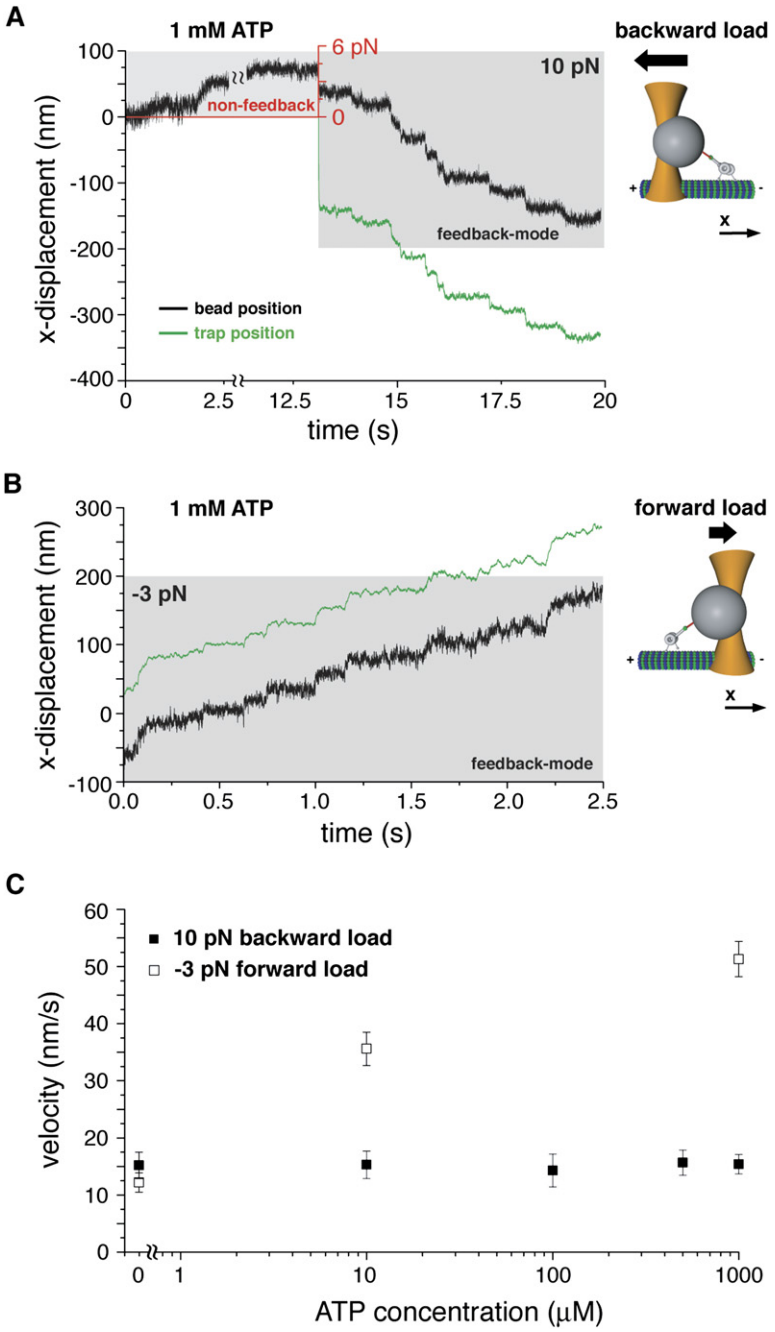

Figure 2. Forced-Backward and Assisted-Forward Movement of Full-Length Dynein in the Presence of ATP Hydrolysis

(A) Optical trapping record of forced-backward movement of $Dyn1_{471kDa}$ under 10 pN superstall force (force-feedback mode, gray-shaded area) following a motor run under increasing rearward load (nonfeedback, upper corner left, the red coordinate system indicates the corresponding force) in the presence of 1 mM ATP (trap stiffness: k = 0.056 pN/nm).

(B) Forward movement of $Dyn1_{471kDa}$ under a −3 pN assisting load and 1 mM ATP (trap stiffness: k = 0.033 pN/nm).

(C) Velocity (absolute values) of $Dyn1_{471kDa}$ movement at 10 pN rearward load (n = 54–77) and −3 pN forward load (n = 52–60), respectively, as a function of ATP concentration. Values are displayed as mean ± SEM.

and in contrast to kinesin under similar salt conditions (Figure S2A), a stalled dynein molecule remained tenaciously bound to a microtubule, often for several minutes, before dissociating (Figure 1C). The stall force of dynein was unchanged when the ATP concentration was decreased from 1 mM to 10 μM (Figure 1D), in contrast to an earlier report on brain cytoplasmic dynein (Mallik et al., 2004) but in agreement with Toba et al. (2006).

We next examined whether dynein would walk backward (toward the microtubule plus end) when the applied load exceeded the stall force, as has been described for kinesin-1 and myosin-V (Carter and Cross, 2005; Gebhardt et al., 2006). To perform this experiment, we applied a constant 10 pN load to the motor using the force-feedback mode of the optical trap (Supplemental Data). When this superstall force was applied in the presence of 1 mM ATP, single dynein molecules moved processively backward toward the microtubule plus end with an average speed of ~15 nm/s (Figures 2A, 2C, and S3). We next tested whether an assisting force (negative force value) directed toward the microtubule minus end could accelerate dynein movement (Figure 2B). However, the

average dynein velocity under a −3 pN assisting load (51 nm/s) was comparable to that observed under unloaded conditions (45 nm/s) (Figures 1E and 2C). By applying different constant forces, we were able to generate a force-velocity curve for dynein spanning between −3 pN and 10 pN force load (Figure 1E).

Force-Induced, Bidirectional Dynein Movement in the Absence of ATP Hydrolysis

To better understand how external forces affect dynein movement, we studied the ATP dependence of movement under an assisting (−3 pN) and superstall (10 pN) force. Remarkably, the velocity of plus-end-directed motion under a superstall load did not depend upon ATP concentration (∼15 nm/s over a wide range of ATP concentrations; Figure 2C). Even in the absence of ATP (ATP/ADP depleted by the enzyme apyrase), a 10 pN rearward pull caused dynein to move processively toward the microtubule plus end (Figures 3A and S4A). In contrast, the velocity of minus-end-directed movement under a −3 pN assisting force was ATP dependent, decreasing by ∼30% at 10 μM ATP (Figure 2C). However, surprisingly, minus-end-directed motion (∼12 nm/s) persisted under nucleotide-free conditions with an applied −3 pN assisting load (Figure 3B).

We next examined the force dependence of nucleotide-independent dynein motility. Without an applied load, all dynein-coated beads that bound to a microtubule (105 beads) did not move, confirming complete nucleotide depletion by apyrase (Supplemental Data). In contrast, with a rearward 10 pN force, ∼90% of the dynein-coated beads that bound to the microtubule exhibited plus-end-directed motion within an ∼10 s window of applied load (56 out of 62). At 7 pN (the stall force), fewer beads (13 out of 25) moved in a similar period of applied force; for beads that failed to move, increasing the load from 7 to 10 pN frequently induced movement (Figure 3A, lower inset). The subset of dynein-coated beads that moved at 7 pN also advanced at a slower velocity (−6.7 ± 1.5 nm/s, mean ± SEM) compared with those that moved at 10 pN (−15.2 ± 2.3 nm/s). At a lower load of 3 pN, only 1 out of 24 beads that bound to the microtubule moved within a 10 s window of applied load. In contrast, with an assisting (minus-end-directed) load of −3 pN, the majority of dynein beads that bound to a microtubule exhibited continuous movement (79 out of 83 beads) (Figures 3B and S4C). Thus, nucleotide-independent movement of dynein is force dependent and much lower forces are necessary to induce movement toward the microtubule minus end than toward the plus end.

We next wished to establish that the force-induced, nucleotide-independent movement was due to dynein stepping, as opposed to detachment of both motor heads, motion along the microtubule axis due to the pull of the optical trap, and then reattachment to the microtubule track (referred to here as "slippage"). To test whether slippage might be occurring, we applied a simultaneous lateral and backward load (9 pN perpendicular and 10 pN parallel to the microtubule axis; Figure 3C). If the dynein motor completely detached from the microtubule, the lateral load would pull the bead away from the axoneme, which should terminate a dynein run (Figure S4B; Gebhardt et al., 2006). However, dynein displayed long processive runs toward the microtubule plus end under such conditions (Figure 3C). Nucleotide-independent dynein movement under forward and backward loads also occurred in small, discrete steps that were similar in size to those observed in the presence of ATP (predominantly ∼8 nm; see next section) (Figure 3D). Large steps that exceeded the maximum step size observed under simultaneous lateral and longitudinal forces (∼30 nm; Figure S4B) and at zero load (∼32 nm; Reck-Peterson et al., 2006) occasionally were observed under 10 pN backward load and might be attributable to slippage, but they constituted a very small fraction of the total steps scored (∼2%; Figure 3D).

In summary, force alone can induce bidirectional dynein stepping in the absence of nucleotide hydrolysis, with a clear asymmetry in the plus- and minus-end directions along the microtubule axis. This behavior distinguishes dynein from kinesin-1 (which has been suggested to require ATP for force-induced backward as well as forward stepping; Carter and Cross, 2005) and myosin-V (which will step backward without ATP hydrolysis but not forward; Gebhardt et al., 2006).

Load-Dependent Stepping Behavior of Cytoplasmic Dynein in the Presence of ATP

To gain additional mechanistic insight into cytoplasmic dynein motility, we analyzed the stepping behavior of single dynein molecules under different constant loads with the force-feedback optical trap in the presence of 1 mM ATP. The displacement traces displayed considerable noise due to thermal fluctuations of the bead-dynein complex (Figure 4). To identify steps with minimal bias, we used a step finding algorithm (Kerssemakers et al., 2006) and verified the ability of this algorithm to detect artificial steps embedded in noise similar to those observed in dynein optical trapping records (Supplemental Data).

One clear feature of the dynein displacement traces is the presence of both forward as well as backward steps at all loads tested (Figure 4; see Figures S5–S7 for additional traces). At the lowest load of 1 pN, dynein predominantly stepped toward the minus end, although ∼30% of the measured steps were in the reverse direction (Figure 4A). This percentage of backward steps is slightly higher than that measured at zero load (∼20%; Reck-Peterson et al., 2006). Thus, even at loads below the stall force, dynein has a relatively weak directional bias. In contrast, using the same optical trap, we rarely observed backward kinesin steps, even at loads approaching stall (Figure S2B). At the stall force of 7 pN, dynein stepping continued, but the numbers of backward and forward steps were approximately equal (Figure S8D), resulting in little or no net movement (Figures 1C and 1E). At the superstall force of 10 pN, ∼75% and ∼25% of the steps were directed toward the microtubule plus and minus

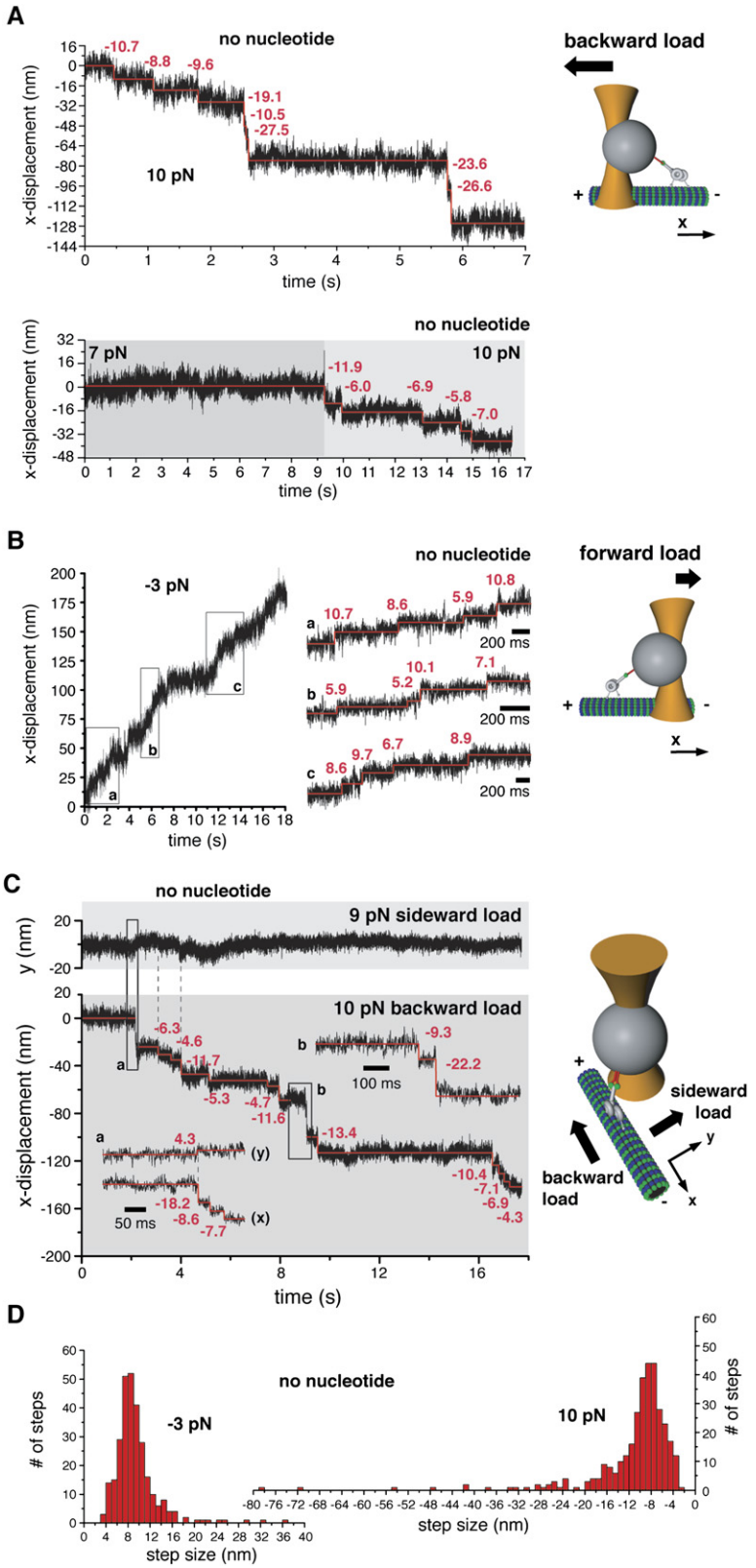

Figure 3. Forced-Backward and Forced-Forward Movement of Full-Length Dynein in the Absence of ATP Hydrolysis

(A) Stepwise backward movement of $Dyn1_{471kDa}$ under 10 pN superstall force in the absence of ATP (trap stiffness: k = 0.055 pN/nm) (upper inset). The lower inset shows an example record of a microtubule-bound $Dyn1_{471kDa}$ motor under stall and superstall loads in the absence of ATP. The motor is tightly bound in rigor for ~9 s under 7 pN stall force without detectable advancing steps and starts to step backward after the application of a 10 pN superstall force (trap stiffness: k = 0.063 pN/nm). The raw data are shown in black and the steps detected by the step-finding program in red.

(B) Optical trapping record of microtubule minus-end-directed movement of $Dyn1_{471kDa}$ under −3 pN forward load in the absence of ATP (trap stiffness: k = 0.055 pN/nm). The trace segments (a, b and c) correspond to the trace sections indicated by the rectangular boxes.

(C) Forced-backward movement of $Dyn1_{471kDa}$ under a simultaneous lateral load of 9 pN and a longitudinal backward load of 10 pN (trap stiffness: k = 0.07 pN/nm). The record shows the displacements of the trapped bead along the microtubule axis (x) and in perpendicular direction (y). The inserted trace segments (a and b) correspond to the trace sections indicated by the rectangular boxes.

(D) Histograms of step sizes for microtubule-minus-end-directed movement under −3 pN assisting load (left, n = 292) and microtubule-plus-end-directed movement under 10 pN rearward load (right, n = 332) in the absence of nucleotide.

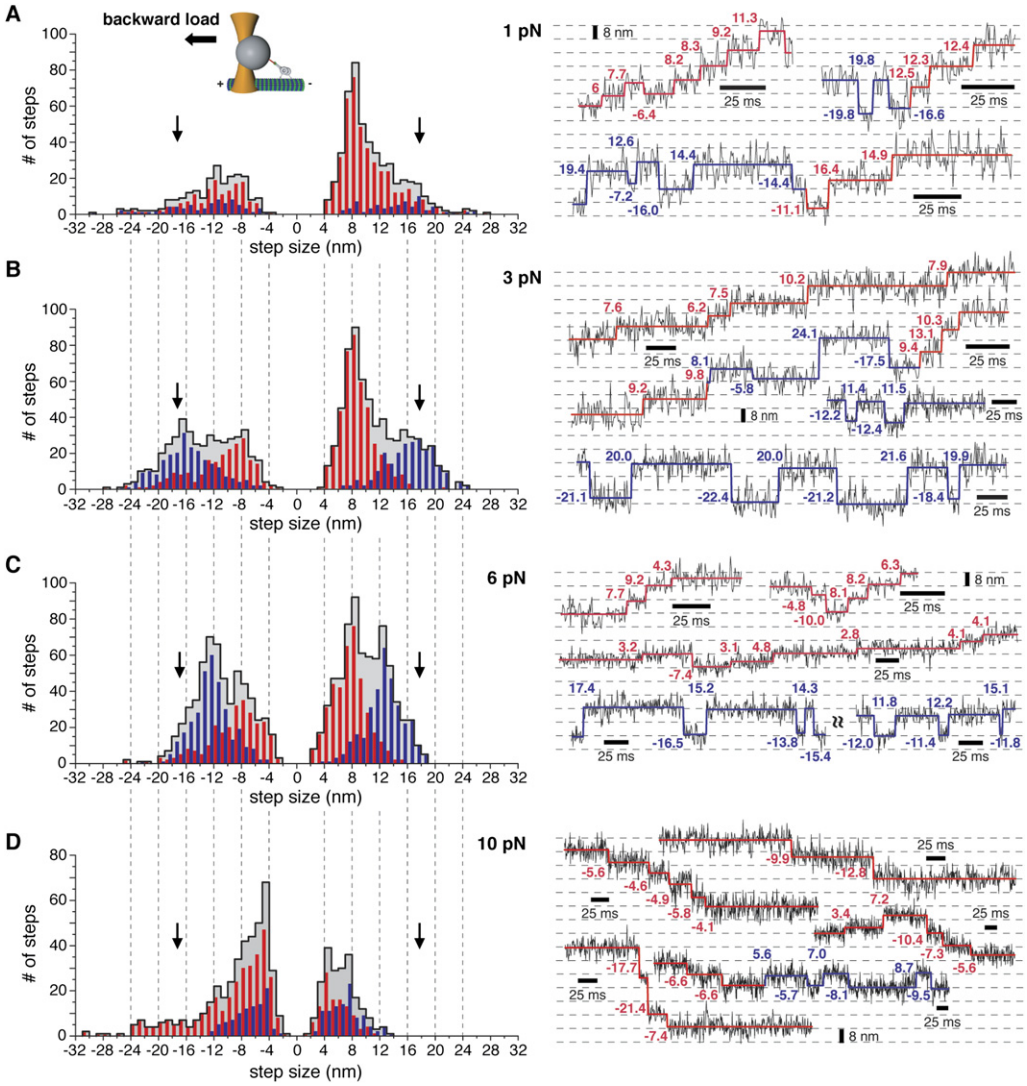

Figure 4. Load-Dependent Stepping Behavior of Full-Length Dynein in the Presence of ATP

(A–D) Histograms of steps sizes and example trace segments measured under 1 pN (n = 716), 3 pN (n = 1104), 6 pN (n = 1314), and 10 pN (n = 642) constant rearward load (force-feedback). The gray-shaded histograms correspond to the combined step size data and the red and blue histogram bars indicate the steps assigned to the advancing and nonadvancing modes, respectively. The raw stepping data are shown in black and the steps detected by the step-finding program in red (advancing mode) and blue (nonadvancing mode). The probability p_b^{adv} for taking a backward step in the advancing mode ($p_f^{adv} + p_b^{adv} = 1$, with p_f^{adv} being the probability for taking a forward step in the advancing mode) at 1, 3, 6, and 10 pN load is 0.26, 0.34, 0.4, and 0.75, respectively (calculated from advancing step size histograms shown in red). The probability $p^{non\text{-}adv}$ for taking any step in the non-advancing mode ($p^{adv} + p^{non\text{-}adv} = 1$, with p^{adv} being the probability for taking any step in the advancing mode) is 0.19, 0.42, 0.5, and 0.31 at 1, 3, 6, and 10 pN, respectively.

ends, respectively (Figure 4D). The minus-end-directed steps at the 10 pN load are driven by ATP turnover since they are not observed under nucleotide-free conditions (Figure 3D).

Our step size histograms also revealed that dynein takes variable sized steps and that load affects the step size distributions (Figure 4, gray-shaded histograms). At 1–3 pN rearward load at 1 mM ATP, the major peak of minus-end-directed steps was centered at 8 nm with a broad shoulder of larger steps (12–24 nm). These large steps are not due to rapid multiple ATP-driven 8 nm steps in succession since the same step size distribution was observed when the motor speed was decreased by lowering the ATP concentration to 10 μM (Figure S9). The peak of backward steps at this load was centered between 8 and 12 nm. This overall distribution is similar to the step size distribution obtained at zero load (Reck-Peterson et al., 2006). At very high loads of 6–10 pN, we observed increased numbers of ~4 nm steps, which were distinguishable from the noise at this high load (Figure 4C,

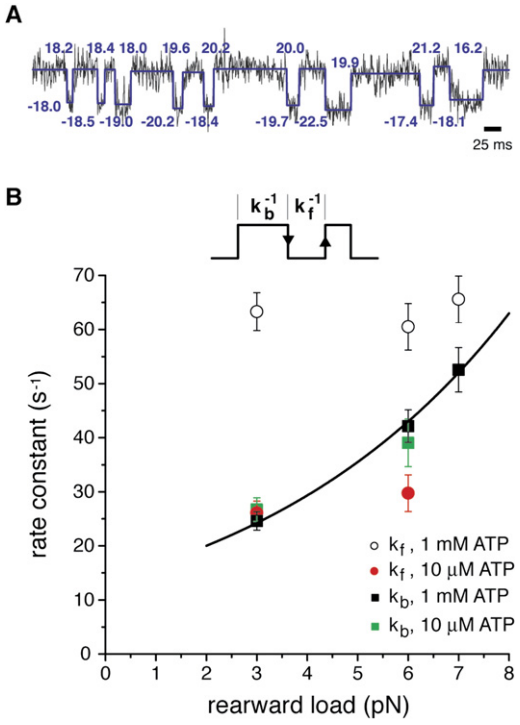

Figure 5. Kinetics of Nonadvancing Stepping of Full-Length Dynein and Load Dependence of Backward Steps

(A) Example record of nonadvancing stepping under 3 pN rearward load.

(B) Rate constants k_f and k_b of nonadvancing forward and backward stepping as a function of load and ATP concentration. The rate constants (mean values) were obtained by cumulative-distribution analysis of the underlying dwell time data (Figure S12). The load dependence of the rate constant k_b at 1 mM ATP (black squares) can be expressed by an exponential function of the form $k_b^0 \exp(Fd/k_BT)$, with $k_b^0 = 13.7 \pm 1.0\ s^{-1}$ and $d = 0.79 \pm 0.05$ nm. Error estimates were calculated as the SD of fit parameters derived from 200 bootstrap samples drawn from the underlying data set.

middle trace and Figure S7). We also observed an appearance of large (12–20 nm) steps in both the forward (minus end) and backward (plus end) direction at intermediate loads of 3–6 pN (Figures 4B and 4C). Further characterization of these large, load-induced steps is described in the next section.

A Nonadvancing Mode of Dynein Stepping Induced by High Loads

An increase in larger steps at higher loads was not anticipated, especially as one prior study reported that the step size of dynein decreases with load (Mallik et al., 2004). Inspection of dynein displacement traces at 3 and 6 pN load revealed that large steps often were contained in long stretches of repeating forward-backward steps that resulted in little or no net displacement of the motor (Figures 4B, 4C, 5A, and S6–S10). Such repetitious forward-backward stepping was uncommon at 1 pN load, where dynein generally took forward steps, interspersed with a single or a few successive (<3) backward steps (Figures 4A and S5).

To examine the characteristics of forward-backward stepping quantitatively, we classified dynein stepping into two categories: an "advancing mode" characterized by two or more successive steps in the same direction (toward either the microtubule minus end or plus end with one intervening reverse step allowed [red lines and histogram bars in Figure 4]), and a "nonadvancing mode" characterized by two or more successive forward-backward steps (blue lines and histogram bars in Figure 4) (see Supplemental Experimental Procedures for more details on classification and statistical analysis). In other words, clustered forward-backward steps are classified as "nonadvancing" while all other stepping is considered to be "advancing." This classification, while perhaps somewhat arbitrary, revealed very different properties for the advancing and nonadvancing modes of dynein stepping. The advancing mode predominated at low loads (1 pN); the step size distribution was centered at 8 nm (with a shoulder at 12 nm) and decreased to 4–8 nm at 6 pN (Figure 4). Interestingly, when load approached the stall force, ~4 nm steps constituted the major peak in the histogram at 7 and 10 pN load (Figures 4D and S8D). These observations indicate that dynein mostly takes small advancing steps and the entire step size distribution shows a modest shift toward smaller size steps with increasing load.

Analysis of the nonadvancing steps revealed several distinct properties from the advancing steps. First, the proportion of nonadvancing steps increased dramatically with load (compare red and blue histograms at 1 and 3 pN in Figure 4). Nonadvancing steps were also larger than advancing steps and accounted for the majority of the 16–20 nm steps at 3 pN. Thus, nonadvancing mode accounts for the unexpected increase in larger steps in the histogram at 3 pN load (Figure 4B). The size of the nonadvancing steps also was affected by load as their distribution shifted to primarily 12–16 nm at 6 pN (Figure 4C). We also observed several nonrandom patterns of nonadvancing stepping (Figure S11). First, a nonadvancing backward step tended to be of the same size as the preceding forward step (at a significantly higher probability than one would expect from the total step size distribution; Figure S11B), suggesting that a large nonadvancing backward step is likely the reversal of a process that led to the forward step. Large forward-backward steps of the same size also tended to cluster together (Figures S11C and S11D), thus returning the bead repeatedly to the same forward and backward positions (see nonadvancing trace segments in Figures 4B, 4C and 5A). The clustering of large similarly sized forward-backward steps also occurred more frequently than statistically expected (Figures S11C and S11D). An interpretation of this nonrandom behavior is that these discrete step sizes reflect particular structural states of the dynein motor that can persist for several ATPase cycles (see Discussion). In contrast, 8 nm forward-backward steps under 3 and 6 pN load did not occur more often than statistically expected (Figures S11C and

S11D). Collectively, these results support the notion that the nonadvancing mode (characterized by large consecutive forward-backward steps) constitutes a distinct pathway from the advancing mode (characterized by mostly 8 nm forward steps; Figure 4).

To gain further insight into dynein's nonadvancing stepping behavior (Figure 5A), we analyzed how load and ATP concentration affect the rates of forward (k_f) and backward (k_b) steps in this nonadvancing mode. The rate constants were obtained by analyzing the dwell times between a forward to a backward step or between a backward to a forward step (Figures 5B and S12). The analysis revealed that k_b increased with increasing load (Figure 5B, black squares), while k_f was relatively unaffected by load (Figure 5B, open circles). The effect of force on k_b can be expressed by a single exponential function of the form $k_b^0 \exp(Fd/k_BT)$, where k_b^0 is the rate constant in the absence of load, d is the transition-state distance along the direction of applied load from the ground state to the transition state, k_B the Boltzmann constant, and T the absolute temperature (Bell, 1978), which yields the parameters $k_b^0 = 13.7 \pm 1.0\ s^{-1}$ and $d = 0.79 \pm 0.05$ nm. The measured transition-state distance is similar to the distance measured for the force-induced unbinding of the myosin-V lead head (0.6 nm, Gebhardt et al., 2006). In contrast, reducing the ATP concentration to 10 μM (a value close to K_m, Figure S9) did not significantly affect k_b (Figure 5B, green squares) but decreased k_f by two-fold (Figure 5B, red circles). In summary, the rate of nonadvancing backward stepping is increased by load but unaffected by ATP, while the rate of nonadvancing forward stepping is unaffected by load and dependent on ATP. These results suggest that the forward step is driven by an ATP-dependent advancement of one of the dynein heads (most likely the trailing head past the leading head), while the backward step represents a detachment of the leading dynein head followed by its reattachment to a rearward binding site.

Role of Dynein's Linker Element in Force Production and Stepping

We next wanted to examine the structural basis of the large dynein steps, which are particularly prevalent in the nonadvancing mode. One model proposed is that large steps may arise when the two dynein motor domains separate into an "extended" conformation (Figure 6A) (Reck-Peterson et al., 2006). Indeed, the large (12–24 nm) nonadvancing forward-backward steps observed at higher loads (3–7 pN) might be due to separation of the dynein heads caused by a mechanical force. According to this model, the maximum head-to-head separation and reach of the dynein dimer in its extended conformation is likely limited by the length of the linker elements interconnecting the dynein heads to the dimerization domain. To test this idea, we examined the stepping behavior of two tail-truncated dynein motors (GST-$Dyn1_{314kDa}$ and GST-$Dyn1_{331kDa}$) that are artificially dimerized by an N-terminal fusion to glutathione S-transferase (GST) (Figure 6B) (Reck-Peterson et al., 2006). In the shorter construct (GST-$Dyn1_{314kDa}$), the distance between the motor heads is likely reduced compared to full-length dynein and the longer construct GST-$Dyn1_{331kDa}$. Both GST-$Dyn1_{314kDa}$ and GST-$Dyn1_{331kDa}$ were previously shown to be processive in a single-molecule TIRF assay, having similar velocities and run lengths to the full-length dynein (Reck-Peterson et al., 2006). GST-$Dyn1_{314kDa}$ is the shortest construct that allows dynein motility; a further 26 aa truncation produced a motor that cannot move and has greatly impaired ATPase activity.

GST-$Dyn1_{331kDa}$ moved in the optical trap and stalled at a rearward load of 4.8 pN (Figure 6C), which is reduced compared to full-length dynein (6.9 pN, $p < 0.001$, two-sided Student's t test). GST-$Dyn1_{331kDa}$ also exhibited a nonadvancing stepping mode, with the distributions of forward-backward steps centered at ~16–20 nm (Figures 6C and S13). The additional 145 aa truncation of dynein's proximal tail to create GST-$Dyn1_{314kDa}$ further reduced the maximal force production (stall force of 4.0 pN, Figure 6D), the percentage of nonadvancing forward-backward stepping at 3 pN, and the number of overall steps that were >12 nm (Figures 6D and S14). These differences between the two truncated dynein constructs suggest that reducing the spacing between the dynein heads limits the ability of the motor to take longer steps and produce greater force. The tail truncation in GST-$Dyn1_{314kD}$, however, did not interfere with force-induced ATP-independent movements toward either the microtubule minus end or plus end (Figure S14). Interestingly, the velocities of nucleotide-independent movement and the forces needed to induce such movement were similar for GST-$Dyn1_{314kD}$ and full-length dynein (see legend to Figure S14), suggesting that the two motors have similar microtubule-binding affinities in the nucleotide-free state.

If head-head spacing is an important determinant for force and step size, then it might be possible to restore these impaired activities in $Dyn1_{314kDa}$ by inserting an artificial linker between the head and beginning of the dimerization domain. We tested this idea by inserting an artificial linker (α-actinin repeats 1 and 2) in between the N terminus of $Dyn1_{314kDa}$ and GST (Figure 6B). The α-actinin insert has a length of ~12 nm and is composed of two rigid, triple-helical bundles linked by an uninterrupted α helix (Kliche et al., 2001). This motor, termed GST-α2-$Dyn1_{314kDa}$, was processive with a primary advancing step size of ~8 nm (Figure 6E) and stalled at an average load of 5.2 pN (Figure 6E), which was significantly higher than the parent GST-$Dyn1_{314kDa}$ construct ($p < 0.001$). Significantly, GST-α2-$Dyn1_{314kDa}$ also displayed a significant number of >12 nm forward-backward steps at 3 pN load in the nonadvancing stepping mode (Figures 6E and S15) compared to $Dyn1_{314kDa}$ (Figure 6D). Thus, GST-α2-$Dyn1_{314kDa}$ appears to more closely resemble the stepping behavior of GST-$Dyn1_{331kDa}$, indicating that the α-actinin repeat sequence partially restored the function of the native dynein linkers that precede the dimerization domain.

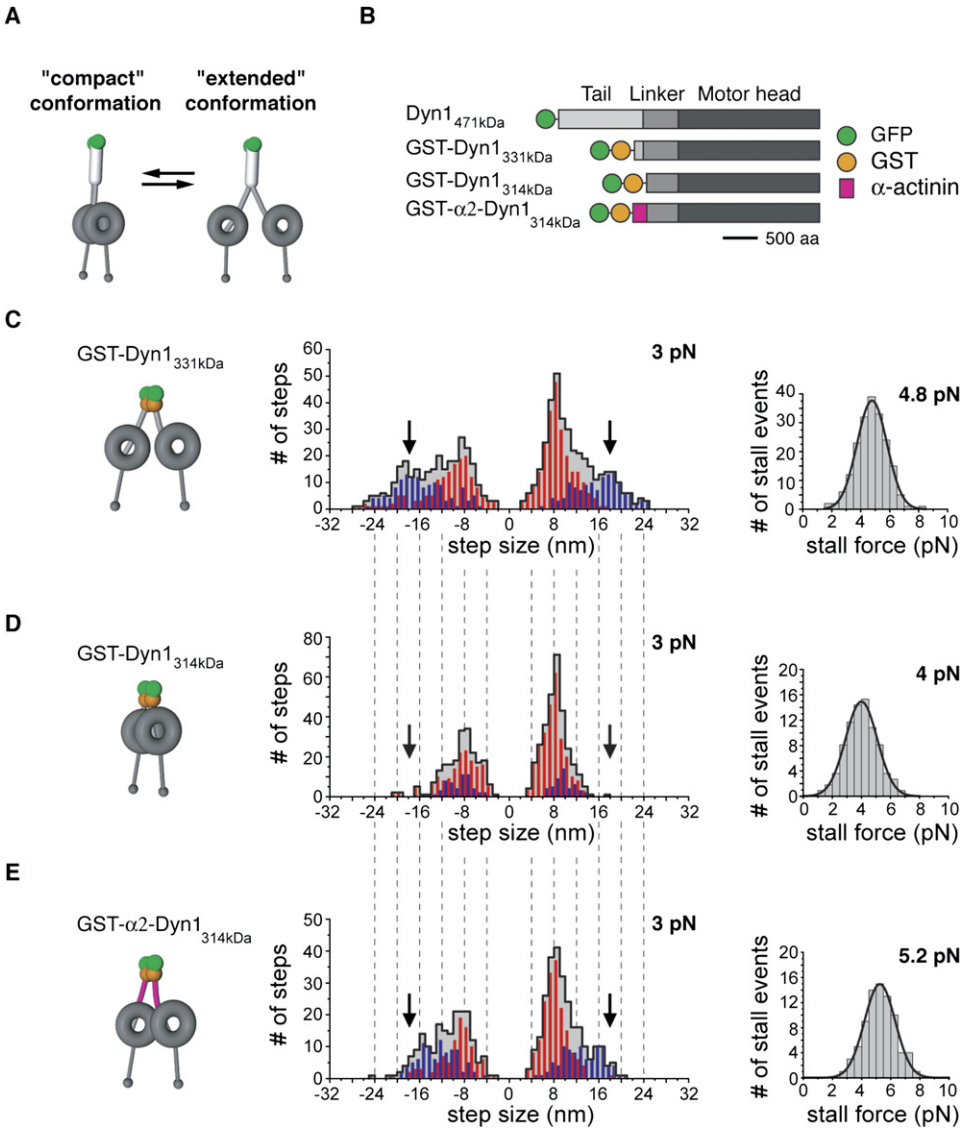

Figure 6. Analysis of Truncated, Artificially Dimerized Dynein Motors in the Optical Trapping Assay and Illustration of the "Compact" and "Extended" Dynein Conformations

(A) Compact and extended conformations of the dynein dimer may explain a wide variation in step size. In its compact state, the two dynein rings are restrained and located in close proximity and perhaps overlapping due to direct head-to-head "interactions" or a "zipping" of the proximal tail. The loss of physical interactions or an "unzipping" of the proximal tail might cause a less restrained extended conformation with an increased head-to-head distance.

(B) Diagram of constructs showing the dynein heavy chain truncations and tags.

(C) Force production and stepping behavior of GST-Dyn1$_{331kDa}$. Left: Schematic of the GST-Dyn1$_{331kDa}$ motor. Center: Histograms of the combined step size data (gray-shaded), classified according to the advancing (red histogram bars) and nonadvancing modes (blue histogram bars) (3 pN force-feedback data, n = 670). Right: Stall force distribution of GST-Dyn1$_{331kDa}$ (4.8 pN ± 1.0 pN; mean ± SD; n = 195).

(D) Force production and stepping behavior of GST-Dyn1$_{314kDa}$. Left: Schematic of the GST-Dyn1$_{314kDa}$ motor. Center: Histograms of the combined, advancing and non-advancing step size data (3 pN force-feedback data, n = 518). Right: Stall force distribution of GST-Dyn1$_{314kDa}$ (4.0 pN ± 1.1 pN; mean ± SD; n = 91).

(E) Force production and stepping behavior of the dynein construct GST-α2-Dyn1$_{314kDa}$ with artificial linker elements. Left: Schematic of the GST-α2-Dyn1$_{314kDa}$ motor. Center: Histograms of the combined, advancing, and nonadvancing step size data (3 pN force-feedback data, n = 457). Right: Stall force distribution of GST-α2-Dyn1$_{314kDa}$ (5.2 pN ± 1.1 pN; mean ± SD; n = 80).

DISCUSSION

Our optical trapping experiments have revealed several force-dependent properties of dynein, which distinguish it from kinesin and myosin. Yeast dynein frequently remains bound to the microtubule for several minutes at stall loads, conditions that tend to dissociate other cytoskeletal motors from their tracks within a few seconds. We also show that dynein is a more irregular stepper (variable step size ranging from 4–24 nm) and its directionality is less robust than that of kinesin-1 and myosin-V. In addition, we demonstrate the unique finding that a mechanical load in the absence of ATP hydrolysis will cause dynein to step processively toward either the minus end or plus end of microtubules, depending upon the direction of the pull. However, there is a significant mechanical asymmetry in the dynein motor, as evidenced by the amount of force required to elicit movement and the ATP dependence of movement in the two directions. The implications of these findings for dynein's mechanism and its biological roles are discussed below.

Models for the Variable Step Sizes and Load-Dependent Stepping of Dynein

The substantial step size variation of yeast cytoplasmic dynein shows similarities and differences with other cytoskeletal motor proteins. Kinesin-1, for example, takes regular 8 nm steps (Svoboda et al., 1993) and takes very few backward steps under substall loads. Myosin-V shows a slight variation in step size around the mean of 36 nm (31–41 nm) due to a diffusional component of the step that enables the leading head to bind to one of three available subunits on the actin filament (Walker et al., 2000; Mehta et al., 1999; Veigel et al., 2002). Dynein, on the other hand, takes a wide range of steps (4–24 nm) and a significant fraction of backward steps as well, which is more akin to the step size variation seen for myosin-VI (~21–51 nm; Rock et al., 2001; Nishikawa et al., 2002). In addition to the occasional backward steps interspersed among the forward steps, our study also demonstrates a previously undescribed nonadvancing forward-backward stepping mode of cytoplasmic dynein at 3–7 pN load. Such repeated forward-backward stepping well below the stall force level is not observed for myosin-V, myosin-VI, or kinesin-1 (Veigel et al., 2002; Rock et al., 2001; Carter and Cross, 2005). It remains possible that this nonadvancing stepping might be a unique feature of yeast cytoplasmic dynein, which could have an increased probability for a transition into the forward-backward stepping mode due to its slower velocity and its lower dissociation rate from the microtubule under load compared with dyneins from other species.

Dynein's variation in step size and nonadvancing stepping at higher loads might be explained by a general structural model in which the motor dimer can adopt either a "compact" or "extended" conformation (Figure 6A). In the "compact" state, the two dynein rings are located in close proximity, perhaps even overlapping, which restrains the reach of the advancing head, resulting in center-of-mass steps of 8 nm (Figure S16A). However, the two motor rings might occasionally separate into an extended conformation that permits a greater reach of the leading head and a consequently larger step size. Much of the step size variation can be explained by the trailing head passing the leading head and landing on various possible binding sites, although ~4 nm steps might be best explained by an inchworm-like progression (Hua et al., 2002) in which the heads do not pass one another (see Figure S16 for models of differently sized stepping). The notion of extended and compact states of the dynein dimer also is suggested by our structure-function studies, which show that a truncation (GST-Dyn1$_{314kDa}$) that reduces the spacing between the two dynein motor domains results in fewer large steps and that insertion of an artificial linker (two α-actinin repeats) after this truncation point partially restores large steps (Figure 6).

Large forward-backward stepping also may be explained by a compact to extended conformational change in the dynein dimer induced by load (Figure 6A). Increased strain on the leading head (caused by the greater head-to-head separation in the extended state) would then favor its detachment and a backward step. This interpretation is supported by our finding that the probability of taking a backward step increases with the size of the preceding forward step (Figure S11A). Our finding of temporally correlated, forward-backward steps of similar sizes (clustering shown in Figures 4 and S6–S11) also raises the possibility of the existence of multiple, discrete extended conformations, which could arise due to different extents of the detachment of the linker element from the dynein ring or the unzipping of the proximal tail.

ATP-Independent Walking: How Force Might Modulate Dynein-Microtubule Interactions

Unexpectedly, we discovered that dynein moves processively toward either the minus end or plus end of microtubules under the constant force of an optical trap in the absence of ATP hydrolysis. The ATP independence of forced-backward movement of dynein differs from that described for kinesin-1, where backward movement under superstall forces has been shown to be dependent upon ATP (Carter and Cross, 2005). In contrast to kinesin and similar to our findings with dynein, Gebhardt et al. (2006) showed that a superstall force will induce backward stepping of myosin-V in an ATP-independent manner. However, the opposite pull (an assisting load) could not induce myosin-V movement in the absence of ATP, in contrast to what we observe for dynein. Thus, our results show that an applied force can coordinate cycles of binding and release of dynein's motor domains in both directions along the microtubule in the absence of nucleotide-derived energy.

Our preferred model for dynein's mechanical asymmetry is based on direct strain sensing by the MTBD (Figure 7, pathways A and B). Unlike myosin and kinesin where the polymer interface is located on the surface of the ATPase

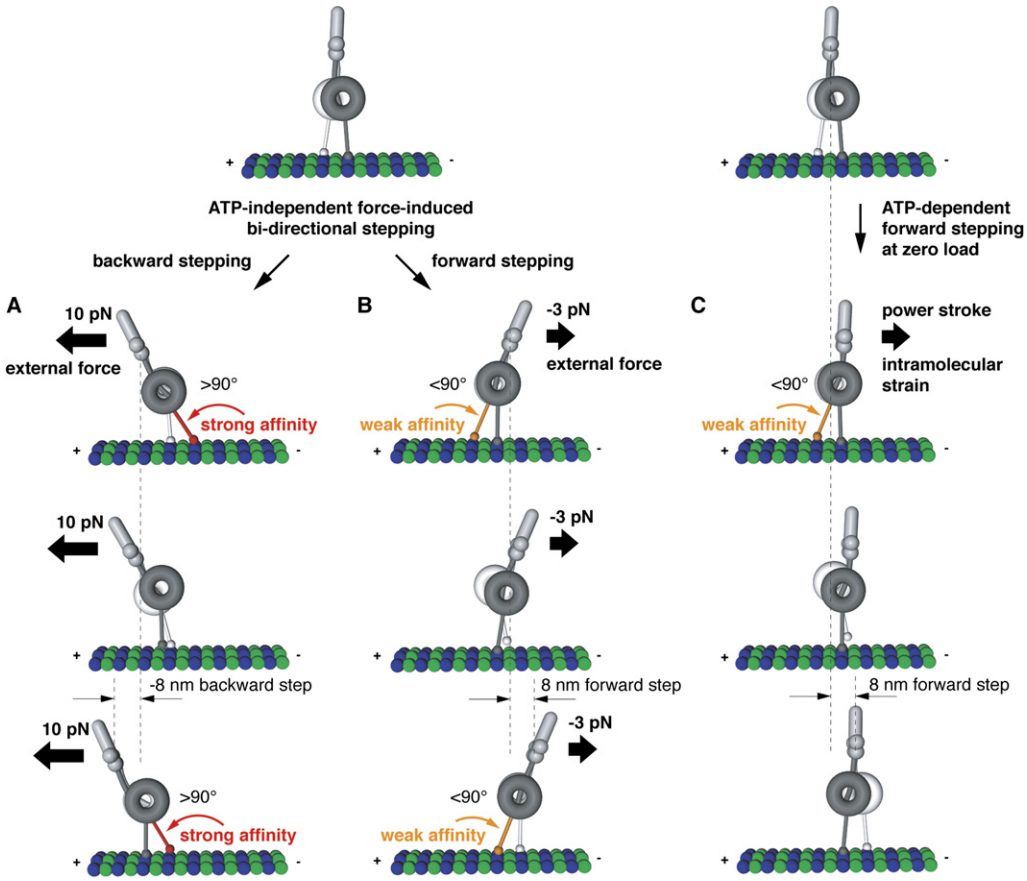

Figure 7. Model for Force-Induced ATP-Independent Bidirectional Stepping and ATP-Dependent Forward Stepping of Cytoplasmic Dynein

Mechanical pathways for force-induced backward (A) and forward (B) stepping and an ATP-dependent pathway for normal forward stepping (C). The key feature proposed for these pathways is a tension-sensing mechanism by the MTBD. In these models, forward deflection of the stalk (induced by external forward load [pathway B] or intramolecular strain provided by a power stroke [pathway C]) weakens the binding affinity of the MTBD in the rear head (indicated by the orange-colored stalks). This mechanism favors rear head detachment and thus helps to keep the dynein heads out-of-phase during continuous movement toward the microtubule minus end. Backward load potentially increases the microtubule-binding affinity of the MTBD in the front head (caused by a load-induced backward deflection of the stalk) (indicated by the red-colored stalk), which explains the large external loads required to induce backward stepping. The size of the α/β tubulin dimers and the length of the stalk and the diameter of the dynein ring are drawn to scale. See the Discussion for more details.

core, dynein's MTBD is situated at the end of an ~10–15 nm antiparallel coiled-coil stalk (Figure 1A). The stalk is likely to bend or change its angle with an applied load, the exact degree of which will depend upon the geometry of the microtubule-dynein-bead complex and the stiffness of the stalk. We postulate that the detachment rate of the MTBD is sensitive to the stalk angle, with angular displacements toward the microtubule minus end (<90°, relative to the microtubule) increasing the dissociation rate. Under an external forward load, the stalk angle of the rear head would move closer to 0°, thus favoring rear head dissociation. After detachment, the forward load would shift the dynein molecule toward the microtubule minus end, allowing the detached head to pass its partner head and rebind to an available tubulin-binding site toward the minus end (Figure 7, pathway B). By repetitive cycles of force-induced rear head detachment, the motor could move toward the minus end in the absence of ATP. In contrast, a rearward load would pull the stalk of the forward head toward 180° (Figure 7, pathway A), a situation that might strengthen its affinity for the microtubule. As this strongly bound front head must detach in order for the motor to step toward the microtubule plus end, this model would explain the higher mechanical load (>7 pN) required to induce plus-end- versus minus-end-directed stepping.

The strain-dependent modulation of the microtubule-binding affinity also might be important for dynein's normal ATP-dependent processive motion (Figure 7, pathway C). In this pathway, we suggest that increased intramolecular strain is induced by an ATP-dependent power stroke in the leading head (reviewed in Spudich, 2006), which

could shift the stalk angle of the trailing head closer to 0° and promote its detachment. Thus, an asymmetric tension-sensing mechanism by the MTBD that favors ATP-dependent (Figures 2C and 5B) rear head detachment could help to keep the dynein heads out-of-phase during processive motion and bias motion toward the microtubule minus end.

Implication of Dynein's Load-Dependent Stepping and Its Biological Role

The force-dependent properties of cytoplasmic dynein are likely adapted for its biological functions. Yeast cytoplasmic dynein produces a stall force that is comparable to kinesin's (Visscher et al., 1999). However, while kinesin dissociates after a few seconds at stall loads, yeast cytoplasmic dynein frequently remains bound tenaciously to the microtubule for minutes without dissociating. These properties would aid yeast dynein's in vivo function in which, most likely, relatively few dyneins pull the large elongating spindle into the daughter cell during cell division.

The ability of yeast dynein to remain microtubule bound and walk backward at superstall forces likely provides new clues for how dynein might operate during spindle positioning and how spindle oscillations might originate (observed along the mother-daughter axis in budding yeast [Yeh et al., 2000] and perpendicular to the anterior-posterior axis of developing *C. elegans* embryos [Pecreaux et al., 2006 and citations therein]). A recent model proposed that spindle oscillations in *C. elegans* embryos are based upon the force-dependent detachment rate of dynein from an astral microtubule (Pecreaux et al., 2006). However, our findings raise another possibility—that dynein could remain attached to an astral microtubule without letting go for several minutes and actively step backward under the opposing forces toward the opposite cell cortex. In addition, dynein's ability to step forward under low assisting force (without detaching or strongly resisting, even under nucleotide-free conditions) would allow "inactive" or "out-of-phase" dynein motors to passively step along the microtubule without strongly interfering with the active motors acting upon the same astral microtubule.

The ability of cytoplasmic dynein to remain microtubule bound and walk backward at superstall forces also makes this motor well suited for a "tug-of-war" with microtubule-plus-end-directed kinesin motor proteins (Gross, 2004; Gennerich and Schild, 2006). Although cytoplasmic dynein does not appear to be involved in organelle transport in yeast, dyneins and kinesins in other eukaryotic organisms appear to be simultaneously bound to various cargos such as organelles, RNP complexes, and chromosomes, generating salutatory bidirectional motion of the cargo (Welte, 2004). At times when kinesin-generated forces exceed those generated by dyneins, dynein could take several steps toward the plus end without letting go of the microtubule; once the opposing force decreases below the stall force level, dynein would immediately be ready to pull again on the microtubule. The low energy barrier difference for dynein stepping in the forward and backward directions (1.3 k_BT at zero load; Figure S17) also might be subject to modification by dynein regulatory proteins. In support of such a possibility, Ross et al. (2006) have recently shown that dynein-dynactin complexes can undergo long movements toward the microtubule plus end.

Another setting in which bidirectional dynein movement may occur is in the flagellum. Nanometer-scale, bidirectional oscillations of microtubule sliding have been described in isolated flagella, and it has been postulated that dynein molecules may have an intrinsic tendency to oscillate (Kamimura and Kamiya, 1989, 1992; Shingyoji et al., 1998). Such oscillations may reflect a mechanical feedback cycle that involves load-induced reversal of dynein stepping, as described in this study. During the rapid bending of cilia/flagella, this would allow dyneins on one side of the axoneme to step passively toward the plus end while dyneins on the opposite side are generating minus-end-directed power strokes. Further work will be required to establish whether axonemal dynein (and also cytoplasmic dyneins from other species) show some of the same biophysical properties that we describe here for yeast cytoplasmic dynein and whether such behavior occurs under the loads that these motors experience in living cells.

EXPERIMENTAL PROCEDURES

Protein Expression and Purification

Full-length ($Dyn1_{471kDa}$) and truncated artificially dimerized cytoplasmic dynein (GST-$Dyn1_{314kDa}$ and GST-$Dyn1_{331kDa}$) from *Saccharomyces cerevisiae* were prepared and purified as described (Reck-Peterson et al., 2006). GST-α2-$Dyn1_{314kDa}$ was constructed from GST-$Dyn1_{314kDa}$ by inserting a DNA fragment encoding residues Q760 to D1002 from the myosin motor-α-actinin fusion construct reported by Kliche et al. (PDB 1G8XI; Kliche et al., 2001). The codon usage was optimized for expression in *S. cerevisiae* and the fragment synthesized by Bio Basic Inc. (Markham, Ontario, Canada). All constructs contained an N-terminal IgG-binding domain and TEV protease cleavage site for protein purification and a terminal GFP for the coupling to anti-GFP antibody-coated latex beads. Before use, all dynein constructs were purified by microtubule affinity (Reck-Peterson et al., 2006).

Optical Trapping Assay

Experiments were performed with a custom-built force-feedback enhanced optical trapping microscope (Supplemental Experimental Procedures). In brief, bead displacement was detected by a quadrant photodiode and recorded at 2 kHz. Carboxylated latex beads (0.92 μm diameter; Invitrogen) were sparsely covered with the GFP-tagged motor proteins via affinity-purified anti-GFP antibodies. The assay solution consisted of 30 mM HEPES (pH 7.2), 2 mM MgAcetate, 1 mM EGTA, 1 mM MgATP, 1 mg/ml casein, 10 mM DTT, 4.5 mg/ml glucose, and an oxygen scavenger system (Supplemental Experimental Procedures). Measurements in the absence of ATP were performed in the same buffer without supplemental ATP in the presence of 10 U/ml apyrase to remove both residual ATP and ADP. Nucleotide-free measurements were undertaken in a specialized ~40 μl flow cell to permit a buffer exchange. Bead displacement did not occur under these conditions unless a mechanical load was applied confirming ATP depletion. After the completion of the force-clamp measurements in the

absence of nucleotides, the buffer solution was exchanged by a solution containing dynein-coated beads and 1 mM supplemental ATP to verify the axoneme polarity by minus-end-directed bead movement. Motor steps (approximate center-of-mass movement of dynein) were determined from the bead displacement records using a step-finding algorithm developed by Kerssemakers et al. (2006), and the details of this analysis are described in the Supplemental Experimental Procedures.

Supplemental Data

Supplemental Data include Supplemental Experimental Procedures and eighteen figures and can be found with this article online at http://www.cell.com/cgi/content/full/131/5/952/DC1/.

ACKNOWLEDGMENTS

The authors wish to thank A. Yildiz, T. Purcell, D. Lörke, O. Akin, E. Lemke, and K. Slep for stimulating discussions; J. Kull for structural advice; J. Kerssemakers and M. Dogterom for generously providing their step-finding program ahead of publication; and T. Purcell for generously providing a Matlab script for generating artificial optical trapping-based motor traces. This work has been supported by the Jane Coffin Childs Foundation (A.G. and A.P.C.), the German Research Foundation (GE 1609/1 [A.G.]), the National Institutes of Health (P01-AR42895 [R.D.V.] and F32-GM67403-02 [S.R.-P.]), the Agouron Institute (A.P.C.), the Leukemia and Lymphoma Society (A.P.C.), and the Howard Hughes Medical Institute.

Received: April 3, 2007
Revised: July 24, 2007
Accepted: October 8, 2007
Published: November 29, 2007

REFERENCES

Asai, D.J., and Koonce, M.P. (2001). The dynein heavy chain: structure, mechanics and evolution. Trends Cell Biol. *11*, 196–202.

Bell, G.I. (1978). Models for the specific adhesion of cells to cells. Science *200*, 618–627.

Burgess, S.A., Walker, M.L., Sakakibara, H., Knight, P.J., and Oiwa, K. (2003). Dynein structure and power stroke. Nature *421*, 715–718.

Carter, N.J., and Cross, R.A. (2005). Mechanics of the kinesin step. Nature *435*, 308–312.

Gebhardt, J.C., Clemen, A.E., Jaud, J., and Rief, M. (2006). Myosin-V is a mechanical ratchet. Proc. Natl. Acad. Sci. USA *103*, 8680–8685.

Gee, M.A., Heuser, J.E., and Vallee, R.B. (1997). An extended microtubule-binding structure within the dynein motor domain. Nature *390*, 636–639.

Gennerich, A., and Schild, D. (2006). Finite-particle tracking reveals submicroscopic-size changes of mitochondria during transport in mitral cell dendrites. Phys. Biol. *3*, 45–53.

Gross, S.P. (2004). Hither and yon: a review of bi-directional microtubule-based transport. Phys. Biol. *1*, R1–R11.

Höök, P., and Vallee, R.B. (2006). The dynein family at a glance. J. Cell Sci. *119*, 4369–4371.

Hua, W., Chung, J., and Gelles, J. (2002). Distinguishing inchworm and hand-over-hand processive kinesin movement by neck rotation measurements. Science *295*, 844–848.

Kamimura, S., and Kamiya, R. (1989). High-frequency nanometre-scale vibration in 'quiescent' flagellar axonemes. Nature *340*, 476–478.

Kamimura, S., and Kamiya, R. (1992). High-frequency vibration in flagellar axonemes with amplitudes reflecting the size of tubulin. J. Cell Biol. *116*, 1443–1454.

Kerssemakers, J.W., Munteanu, E.L., Laan, L., Noetzel, T.L., Janson, M.E., and Dogterom, M. (2006). Assembly dynamics of microtubules at molecular resolution. Nature *442*, 709–712.

King, S.J., and Schroer, T.A. (2000). Dynactin increases the processivity of the cytoplasmic dynein motor. Nat. Cell Biol. *2*, 20–24.

Kliche, W., Fujita-Becker, S., Kollmar, M., Manstein, D.J., and Kull, F.J. (2001). Structure of a genetically engineered molecular motor. EMBO J. *20*, 40–46.

Kon, T., Nishiura, M., Ohkura, R., Toyoshima, Y.Y., and Sutoh, K. (2004). Distinct functions of nucleotide-binding/hydrolysis sites in the four AAA modules of cytoplasmic dynein. Biochemistry *43*, 11266–11274.

Kon, T., Mogami, T., Ohkura, R., Nishiura, M., and Sutoh, K. (2005). ATP hydrolysis cycle-dependent tail motions in cytoplasmic dynein. Nat. Struct. Mol. Biol. *12*, 513–519.

Koonce, M.P., and Tikhonenko, I. (2000). Functional elements within the dynein microtubule-binding domain. Mol. Biol. Cell *11*, 523–529.

Mallik, R., Carter, B.C., Lex, S.A., King, S.J., and Gross, S.P. (2004). Cytoplasmic dynein functions as a gear in response to load. Nature *427*, 649–652.

Mallik, R., Petrov, D., Lex, S.A., King, S.J., and Gross, S.P. (2005). Building complexity: an in vitro study of cytoplasmic dynein with in vivo implications. Curr. Biol. *23*, 2075–2085.

Mehta, A.D., Rock, R.S., Rief, M., Spudich, J.A., Mooseker, M.S., and Cheney, R.E. (1999). Myosin-V is a processive actin-based motor. Nature *400*, 590–593.

Nishikawa, S., Homma, K., Komori, Y., Iwaki, M., Wazawa, T., Hikikoshi Iwane, A., Saito, J., Ikebe, R., Katayama, E., Yanagida, T., and Ikebe, M. (2002). Class VI myosin moves processively along actin filaments backward with large steps. Biochem. Biophys. Res. Commun. *290*, 311–317.

Ogura, T., and Wilkinson, A.J. (2001). AAA+ superfamily of ATPases: common structure - diverse function. Genes Cells *6*, 575–597.

Pecreaux, J., Röper, J.C., Kruse, K., Jülicher, F., Hyman, A.A., Grill, S.W., and Howard, J. (2006). Spindle oscillations during asymmetric cell division require a threshold number of active cortical force generators. Curr. Biol. *16*, 2111–2122.

Reck-Peterson, S.L., and Vale, R.D. (2004). Molecular dissection of the roles of nucleotide binding and hydrolysis in dynein's AAA domains in Saccharomyces cerevisiae. Proc. Natl. Acad. Sci. USA *101*, 1491–1495.

Reck-Peterson, S.L., Yildiz, Y., Carter, A.P., Gennerich, A., Zhang, N., and Vale, R.D. (2006). Single molecule analysis of dynein processivity and stepping behavior. Cell *126*, 335–348.

Rock, R.S., Rice, S.E., Wells, A.L., Purcell, T.J., Spudich, J.A., and Sweeney, H.L. (2001). Myosin VI is a processive motor with a large step size. Proc. Natl. Acad. Sci. USA *98*, 13655–13659.

Ross, J.L., Wallace, K., Shuman, H., Goldman, Y.E., and Holzbaur, E.L. (2006). Processive bidirectional motion of dynein-dynactin complexes in vitro. Nat. Cell Biol. *8*, 562–570.

Shingyoji, C., Higuchi, H., Yoshimura, M., Katayama, E., and Yanagida, T. (1998). Dynein arms are oscillating force generators. Nature *393*, 711–714.

Silvanovich, A., Li, M.G., Serr, M., Mische, S., and Hays, T.S. (2003). The third P-loop domain in cytoplasmic dynein heavy chain is essential for dynein motor function and ATP-sensitive microtubule binding. Mol. Biol. Cell *14*, 1355–1365.

Spudich, J.A. (2006). Molecular motors take tension in stride. Cell *126*, 242–244.

Svoboda, K., Schmidt, C.F., Schnapp, B.J., and Block, S.M. (1993). Direct observation of kinesin stepping by optical trapping interferometry. Nature *365*, 721–727.

Takahashi, Y., Edamatsu, M., and Toyoshima, Y.Y. (2004). Multiple ATP-hydrolyzing sites that potentially function in cytoplasmic dynein. Proc. Natl. Acad. Sci. USA *101*, 12865–12869.

Toba, S., Watanabe, T.M., Yamaguchi-Okimoto, L., Toyoshima, Y.Y., and Higuchi, H. (2006). Overlapping hand-over-hand mechanism of single molecular motility of cytoplasmic dynein. Proc. Natl. Acad. Sci. USA *103*, 5741–5745.

Vale, R.D. (2003). The Molecular motor toolbox for intracellular transport. Cell *112*, 467–480.

Vallee, R.B., Williams, J.C., Varma, D., and Barnhart, L.E. (2004). Dynein: An ancient motor protein involved in multiple modes of transport. J. Neurobiol. *58*, 189–200.

Veigel, C., Wang, F., Bartoo, M.L., Sellers, J.R., and Molloy, J.E. (2002). The gated gait of the processive molecular motor, myosin V. Nat. Cell Biol. *4*, 59–65.

Visscher, K., Schnitzer, M.J., and Block, S.M. (1999). Single kinesin molecules studied with a molecular force clamp. Nature *400*, 184–189.

Walker, M.L., Burgess, S.A., Sellers, J.R., Wang, F., Hammer, J.A., 3rd, Trinick, J., and Knight, P.J. (2000). Two-headed binding of a processive myosin to F-actin. Nature *405*, 804–807.

Wang, Z., Khan, S., and Sheetz, M.P. (1995). Single cytoplasmic dynein molecule movements: Characterization and comparison with kinesin. Biophys. J. *69*, 2011–2023.

Welte, M.A. (2004). Bidirectional transport along microtubules. Curr. Biol. *14*, R525–R537.

Yeh, E., Yang, C., Chin, E., Maddox, P., Salmon, E.D., Lew, D.J., and Bloom, K. (2000). Dynamic positioning of mitotic spindles in yeast: role of microtubule motors and cortical determinants. Mol. Biol. Cell *11*, 3949–3961.

Cell, Volume *131*

Supplemental Data

Force-Induced Bidirectional Stepping of Cytoplasmic Dynein

Arne Gennerich, Andrew P. Carter, Samara L. Reck-Peterson, and Ronald D. Vale

Supplemental Experimental Procedures

Optical Trapping Assay

Experiments were performed at 25 ± 1 °C with a custom-built force-feedback enhanced optical trapping microscope. In brief, a near-infrared laser beam (Nd:YVO_4, 1,064 nm; Spectra Physics) was coupled into a custom-built inverted microscope equipped with a 63x/1.4 NA oil-immersion objective (Plan-Apochromat, Carl Zeiss, Thornwood, NY) and split into horizontally and vertically polarized light to generate two independently controllable traps (trap 1 and trap 2). The beam of trap 1 was steered by a computer-controlled mirror system and was used to capture a bead anywhere in the object field and to transfer the captured bead to trap 2 in the object center. The position of trap 2 was controlled by a DSP-board (M67, Innovative Integration, Simi Valley, CA) via a two-axis acousto-optic deflection system (DTD-274HA6, IntraAction, Bellwood, IL) and restricted to a 1.5x1.5 μm area located in the center of the object field. Trap 2 was integrated into a position feedback loop controlled by the DSP-board and used for the measurements. Force-feedback was operational in an area of ± 200 nm along both the *x*- and *y*-axis of the object field. Bead displacement was detected by a quadrant photodiode and recorded at 2 kHz. Trap stiffness was calibrated for each trapped bead from the amplitude of the thermal diffusion. Before each experiment, the trapped bead was scanned along the *x*-axis (or both the *x*- and *y*-axis in case of trapping measurements under simultaneous lateral and longitudinal forces) of the object field across the detection region to obtain the detector's response. A trapped bead was then positioned over a rhodamine-labeled sea urchin sperm flagellar axoneme that was immobilized onto a coverslip and aligned with the *x*-axis of the object field (coincides with the *x*-axis of the position detector).

Carboxylated latex beads (0.92 μm diameter; Invitrogen) were sparsely covered with the GFP-tagged motor proteins via affinity-purified anti-GFP antibodies (Tomishige et al., 2002). Experiments were performed at dilutions at which the fraction of beads moving was ≤ 0.3 to ensure measurements on a single-molecule level (motor aggregation has been previously excluded by single- and two-step photobleaching experiments of the GFP-tagged dynein motors; Reck-Peterson et al., 2006). At this dynein-bead ratio, the probability that a bead has two or more bound motors is <0.05 (see legend to Figure S1 for the equations underlying this calculation). However, the probability that two randomly attached dynein molecules are positioned close enough to one another that they could simultaneously bind to a microtubule is negligible. Assuming a random distribution of motors on the bead surface (Svoboda and Block, 1994), the upper probability limit can be estimated by $(\pi dl/\pi d^2)^2 = (l/d)^2$, with l and d being the reach of

the motor and the bead diameter, respectively. The reach of the full-length dynein molecule can be estimated from the putative length of the stalk and the diameter of the dynein head ring (~15 nm each, Burgess et al., 2003), the length of the detached linker element (~10 nm, Burgess et al., 2003), the approximate length of the tail domain (~30 nm, Fan and Amos, 2001) and the size of the GFP and α-GFP antibody complex (~15 nm). The combined lengths result in a dynein reach of ~85 nm and together with an average bead diameter of 920 nm, this calculation yields an estimation of $p < 0.009$. Collectively, there is a >99% probability that the observed movements are due to single dynein molecules at the dynein-bead ratios used.

Velocities were obtained from line fits to the displacement traces of the beads moving under constant load from the force-feedback controlled optical trap. The measured velocities (Figure 1E) are slightly lower than reported for zero load in a single molecule fluorescence assay (Reck-Petersen et al., 2006) due to the lower salt concentration used in the optical trap assay (see main text). Stall forces were determined by multiplying the trap stiffness by the mean maximum distance reached and sustained for more than 10 s. To minimize errors in stall force measurements, trap stiffness was set to ~0.07 pN/nm, ~0.05 pN/nm or ~0.04 pN/nm for full-length dynein (7 pN stall force), GST-Dyn1$_{331kDa}$ (4.8 pN stall force) or GST-α2-Dyn1$_{314kDa}$ (5.2 pN stall force), and GST-Dyn1$_{314kDa}$ (4 pN stall force), respectively, so that each construct stalled at an average bead-trap separation of ~100 nm (Block et al., 2003).

Measurements were performed in a ~10 µl flow cell constructed by placing two strips of double-sided sticky tape between a standard microscope slide and a 160 µm thick 18 mm x 18 mm cover slip to form a channel. Before use, cover slips were acid-washed (Pierce et al., 1999). The assay solution consisted of 30 mM HEPES (pH 7.2), 2 mM MgAcetate, 1 mM EGTA, 1 mM MgATP, 1 mg/ml casein, 10 mM DTT, 4.5 mg/ml glucose, and an oxygen scavenger system (Yildiz et al., 2003). Flow cells were finally sealed with nail polish. The measurements presented in Figures 1D and 2C (stall force and velocity as a function of ATP concentration) were performed with the same buffer but with varying ATP concentrations and supplemented with an ATP regeneration system (2 mM phosphoenolpyruvate and 0.1 mg/ml pyruvate kinase).

Measurements in the absence of ATP were done in a specialized ~40 µl flow cell constructed in the same way as the 10 µl flow cell (see above) but using a 24 mm x 600 mm coverslip and sealed with two-component epoxy glue. Two 1 mm holes were drilled into the microscope slide close to the opposite sealed edges of the flow cell to allow a buffer exchange via a pipette while the flow cell was tightly mounted to the microscope stage and without moving the microscope collimator (to prevent any µm-scale slide displacements during buffer exchange). ATP free measurements were undertaken in assay buffer containing Dyn1$_{471kDa}$-coated beads, no supplemental ATP and 10 U/ml apyrase to remove both residual ATP and ADP. After motor binding (judged by the decrease in Brownian noise of the trapped bead), longitudinal loads of ±3 and ±10 pN were applied to probe the motor's response to external force. Immediately after the activation of the force-feedback routine, the computer-controlled stage was displaced along the *x*-axis to move the axoneme-bound bead to the opposite edge of the detection area (to permit the measurement of the bead movement across the entire detection range). Experiments with a simultaneous lateral load of 9 pN and a longitudinal backward load of 10 pN were performed by displacing the axoneme-bound bead along both the *x*- and *y*-axis to the corner of the detection area followed by activation of a two-dimensional force-feedback routine. After the completion

of the force-clamp measurements in the absence of nucleotides, the buffer solution was exchanged by a solution containing dynein-coated beads and 1 mM supplemental ATP to verify the axoneme polarity by minus-end-directed bead movement.

Measurement of dynein step sizes

Motor steps (approximate center-of-mass movement of dynein) were determined from the bead displacement records using a step-finding algorithm developed by Kerssemakers et al. (2006). This algorithm assumes that steps are hidden in normal-distributed noise but makes no assumptions about steps sizes and durations. The use of the algorithm has been demonstrated for reliably detecting different sized steps in microtubule-assembly-based traces (Kerssemakers et al., 2006) as well as kinesin-induced microtubule-gliding displacement records (Leduc et al., 2007). The sole user-supplied input parameter is a rough estimate of the number of hidden steps. This parameter was chosen so that the algorithm appeared to slightly "overfit" the data (Figure S18C) (Kerssemakers et al., 2006). The resulting data were than visually screened and only those steps that could be visually separated from noise were included in the step size histograms. Using this method, we were typically able to assign step sizes to 40-80% of a given dynein run.

To test the reliability of this step-finding method, we analyzed artificial optical-trapping based stepping traces (Figure S18). We performed computer simulations to generate stepping traces with step sizes of known size, number and stepping rates and then superimposed the generated traces with normal-distributed noise. The traces were than passed through a one-pole Butterworth low-pass filter to create a Lorentzian power spectrum with a corner frequency similar to the characteristic corner frequency of the Lorentzian power spectrum of the trapped bead (Sheetz, 1998). In addition, the noise amplitude of the unfiltered stepping traces was adjusted to obtain filtered traces with a noise amplitude similar to the amplitude seen in the experimental traces.

We first simulated and analyzed 1 pN optical trapping traces with hidden 8 nm forward and backward steps by adjusting the final noise amplitude to 5.8 nm (SD; experimental measured value) and assuming a spring constant of $k = 0.05\,\mathrm{pN/nm}$ (frequently used for 1 pN measurements), which corresponds to a corner frequency of the Lorentzian power spectrum of ~1000 Hz ($f_c = k/6\pi^2\eta d$, with $d = 920\,\mathrm{nm}$ and $\eta = 8.9 \cdot 10^{-10}\,\mathrm{pNs/nm^2}$ being the dynamic viscosity of water at 25 °C). The rate of stepping was set to 20 steps per second, which is close to k_{cat} measured under saturating ATP conditions (16/s, Reck-Peterson et al., 2006) and also close to the effective rate $k_f k_b/(k_f + k_b)$ of ATP-driven forward stepping in the non-advancing mode (13-25/s; Figure 5B). The result of the step size analysis of generated traces with 569 hidden 8 nm steps is shown in Figure S18A. Our step size analysis, which could reliably find 80% of the simulated steps, yielded 75% forward steps, in agreement with the fraction of simulated forward steps (71%). The analysis further revealed a predominant forward step size of 8 nm (average value of 8.05 nm) and a minor fraction of 16 nm steps (2.7% of all forward steps) caused by missed 8 nm steps. This analysis indicates that the significant fractions of dynein steps >8 nm observed under 1 pN load and 1 mM ATP (~40%; Figure 4A) are not due to rapid multiple ATP-driven 8 nm steps in succession.

We next tested our step size analysis for detecting a mixture of different sized forward and backward steps under the increased noise level found at 1 pN load. We simulated and analyzed

traces with 1068 hidden forward and backward steps of 4, 8, 12 and 16 nm size (same underlying parameters as described above) (Figure S18B and S18C). Our analysis, which could reliably find 66% of the simulated steps, yielded 71% forward steps, well in agreement with the fraction of simulated forward steps (70%). To determine the step sizes of the simulated data we fitted multiple Gaussian functions (with a uniform distribution width) to the step size histogram of forward steps (Figure S18B). This analysis revealed a major forward step size of 8 nm (46%) and fractions of 5 nm (15%), 12 nm (21%) and 16 nm steps (16%) as well as a minor negligible fraction of 20 nm steps (<2.5%) caused by rapid multiple small steps in succession (Figure S18C, trace segment c). These results agree well with the fractions of simulated 8 nm (53%), 12 nm (16%) and 16 nm steps (12%). However, this analysis also shows that the simulated fraction of 4 nm steps (19%) is slightly skewed toward 5 nm in the step size histogram as a result of the lower detection precision for steps that have a size close or smaller than the noise amplitude (Kerssemakers et al., 2006). Collectively, our simulations show that populations of different sized dynein steps (as seen in our traces) can be reliably measured at 1 mM ATP even under the increased noise levels found at the lowest load of 1 pN using the step-finding method described above.

Classification of advancing and non-advancing stepping

All measurable steps in a dynein trace were assigned by the methods described above. A forward step followed by a step in the reverse direction is called a forward-backward step; two or more of such forward-backward steps in succession are classified as "non-advancing" while all other stepping is considered to be "advancing". A single reverse step interspersed among advancing steps is still assigned to the "advancing" model. The steps that occurred at the beginning or the end of non-advancing stepping were assigned to either the advancing or non-advancing stepping mode depending on their size: A backward step at the beginning or end of a series of non-advancing steps was assigned to the non-advancing stepping mode if its size was similar to the size of the following or preceding forward step (e.g. –17.4 nm step in Figure S6, third trace segment from the bottom); if the beginning or end step was a forward step, then same criteria applied (assigned to the non-advancing mode if the size was similar to the following or preceding backward step). If these criteria did not apply, then the beginning or end step was assigned to the advancing stepping mode.

Supplemental References

Block, S.M., Asbury, C.L., Shaevitz, J.W., and Lang, M.J. (2003). Probing the kinesin reaction cycle with a 2D optical force clamp. Proc. Natl. Acad. Sci. USA *100*, 2351-2356.

Burgess, S.A., Walker, M.L., Sakakibara, H., Knight, P.J., and Oiwa, K. (2003). Dynein structure and power stroke. Nature *421*, 715-718.

Fan, J., and Amos, L.A. (2001). Antibodies to cytoplasmic dynein heavy chain map the surface and inhibit motility. J. Mol. Biol. *307*, 1317-1327.

Gebhardt, J.C., Clemen, A.E., Jaud, J., and Rief, M. (2006). Myosin-V is a mechanical ratchet. Proc. Natl. Acad. Sci. USA *103*, 8680-8685.

Kerssemakers, J.W., Munteanu, E.L., Laan ,L., Noetzel, T.L., Janson, M.E., and Dogterom, M. (2006). Assembly dynamics of microtubules at molecular resolution. Nature *442*, 709-712.

Leduc, C., Ruhnow, F., Howard, J., and Diez, S. (2007). Detection of fractional steps in cargo movement by the collective operation of kinesin-1 motors. Proc. Natl. Acad. Sci. USA *104*, 10847-10852.

Nishiyama, M., Higuchi, H., and Yanagida, T. (2002). Chemomechanical coupling of the forward and backward steps of single kinesin molecules. Nat. Cell Biol. *4*, 790-797.

Pierce, D.W., Hom-Booher, N., Otsuka, A.J., Vale, R.D. (1999). Single-molecule behavior of monomeric and heteromeric kinesins. Biochemistry *38*, 5412-5421.

Reck-Peterson, S.L., Yildiz, Y., Carter, A.P., Gennerich, A., Zhang, N., and Vale, R.D. (2006). Single molecule analysis of dynein processivity and stepping behavior. Cell *126*, 335-348.

Scheetz, M. (Editor). (1998). Laser Tweezers in Biology. (New York: Academic Press).

Schwarz, G. (1978). Estimating the dimension of a model. Ann. Stat. *6*, 461-464.

Svoboda, K., and Block, S.M. (1994). Force and velocity measured for single kinesin molecules. Cell *77*,773–784.

Tomishige, M., Klopfenstein, D.R., Vale, R.D. (2002). Conversion of Unc104/KIF1A kinesin into a processive motor after dimerization. Science *297*, 2263-2267.

Yildiz, A., Forkey, J.N., McKinney, S.A., Ha, T., Goldman, Y.E., and Selvin, P.R. (2003). Myosin V walks hand-over-hand: single fluorophore imaging with 1.5-nm localization. Science *300*, 2061-2065.

Figure S1. Fraction of dynein-coated beads binding to and moving along axonemes as a function of the relative motor concentration. The bead concentration was kept constant for all measurements, whereas the motor concentration was varied ($N = 224$ total measurements; $n = 32 - 48$ at each concentration). The solid line represents the fit to the Poisson distribution $1 - \exp(-\lambda C)$ for one or more motor molecules, where C is the relative motor concentration and λ is a fit parameter (Svoboda and Block, 1994) (reduced $\chi^2 = 0.1$). The dotted line represents the fit to the distribution $1 - \exp(-\lambda C) - (\lambda C)\exp(-\lambda C)$ for two or more molecules (reduced $\chi^2 = 2.1$). Data values are displayed as the mean ± the square root of $(f[1-f]/N)$, with N being the number of beads tested.

Figure S2. Processive movement of single K560-GFP molecules in the optical trapping microscope used in this study. (A) Single motor runs against increasing rearward loads (non-feedback optical trapping mode, k = 0.057 pN/nm). The kinesin stall force is ~ 7 pN. (B) Processive movement of K560-GFP (Tomishige et al., 2002) under a constant rearward load of 6 pN (force-feedback mode; k = 0.06 pN/nm) showing 8 nm forward steps only (unlike dynein). The filtered bead position (20-point window, red trace) is superimposed on the unfiltered position (black trace). The assay solution consisted of BRB80 buffer (80 mM PIPES, 2 mM $MgCl_2$, 1 mM EGTA, pH 6.8), 1 mM MgATP, 1 mg/ml casein, 10 mM DTT, 4.5 mg/ml glucose, and an oxygen scavenger system (Yildiz et al., 2003).

Figure S3. Force-induced microtubule plus-end-directed stepping of full-length dynein under 10 pN superstall force and 1 mM ATP. (A) Optical trapping record of processive forward and forced-backward movement of dynein under substall and superstall loads in the presence of 1 mM ATP. In this experiment, we first applied a modest rearward load (2 pN, left), which allowed the motor to move to the edge of the feedback-controlled trapping area (shaded areas), and then switched to a rearward load of 10 pN (right) (trap stiffness: $k = 0.068$ pN/nm). The inserted trace segments (a and b, respectively) correspond to the trace sections indicated by the rectangular boxes. The raw data is shown in black and the steps detected by the step finding program in red. (B, C) Further example displacement records showing microtubule plus-end-directed movement under a constant backward load of 10 pN in the presence of 1 mM ATP (trap stiffness: $k = 0.056$ pN/nm). Additional stepping data is shown in Figure 2 of the paper.

Figure S4. Force-induced microtubule plus- and minus-end-directed stepping of full-length dynein in the absence of ATP binding and hydrolysis. (A) Example records of forced-backward stepping at 10 pN rearward load in the absence of ATP (trap stiffness: $k = 0.06$ pN/nm). The trace segments marked by a and b correspond to the parts of the displacement trace shown above. (B) Example record of ATP-independent forced-backward movement of dynein under a simultaneous lateral load of 9 pN and a longitudinal backward load of 10 pN (trap stiffness**:** $k = 0.06$ pN/nm). The record shows the displacements of the trapped bead along the microtubule axis (x) and in perpendicular direction (y). (C) Force-induced ATP-independent microtubule minus-end-directed stepping under –3 pN forward load (trap stiffness: $k = 0.06$ pN/nm). (A-C) Bead positions (raw data) are drawn in black and the steps detected by the step finding program in red. Additional stepping data is shown in Figure 3 of the paper.

Figure S5. Dynein stepping at 1 pN constant rearward load. The raw data is shown in black

and the steps detected by the step finding program in red (advancing mode). Additional stepping data is shown in Figure 4 of the paper.

Figure S6. Dynein stepping at 3 pN constant rearward load. The raw data is shown in black and the steps detected by the step finding program in red (advancing mode) and blue (non-advancing mode), respectively. Additional stepping data is shown in Figure 4 of the paper.

Figure S7. Dynein stepping at 6 pN constant rearward load. The raw data is shown in black and the steps detected by the step finding program in red (advancing mode) and blue (non-advancing mode), respectively. Additional stepping data is shown in Figure 4 of the paper.

Figure S8. Histograms of step sizes of full-length dynein as a function of load
(A-E) Histograms of step sizes measured under 1 pN (N=716), 3 pN (N=1104), 6 pN (N=1314), 7 pN (N=627) and 10 pN (N=642) constant rearward load. Steps were categorized and assigned to the advancing mode (red histogram bars) and non-advancing mode (blue histogram bars). p_b^{adv} and $p^{\text{non-adv}}$ correspond to the probabilities for taking a backward step b in the advancing mode ($p_f^{\text{adv}} + p_b^{\text{adv}} = 1$, with p_f^{adv} being the probability for taking a forward step f in the advancing mode) and for taking any step in the non-advancing mode ($p^{\text{adv}} + p^{\text{non-adv}} = 1$, with p^{adv} being the probability for taking any step in the advancing mode). The same data is also shown in Figure 4 embedded in the total step size histogram. The stall force (7 pN) data is shown here but not in Figure 4.

Figure S9. Stepping of full-length dynein under limiting ATP conditions
To evaluate whether the optical trapping measurements undertaken at a saturating ATP concentration (1 mM) resulted in an overestimation of the fraction of large (> 8 nm) steps (as a result of missed events), we generated and analyzed artificial stepping traces (Figure S18) and performed a step size analysis under limiting ATP conditions to slow the dynein stepping rate. Under 3 pN backward load (force-feedback), a low ATP concentration of 10 μM causes full-length dynein to advance at an average velocity of ~10 nm/s, which is ~50% slower compared to the velocity at a saturating ATP concentration (22 nm/s, 1 mM; Figure 1E). A concentration of 10 μM ATP is thus reasonably close to the K_m. (A) Step size histogram acquired at 3 pN rearward load and 10 μM ATP (n = 1088). The grey-shaded histogram corresponds to the combined step size data and the red and blue histogram bars indicate the steps assigned to the advancing mode ($p_b^{\text{adv}} = 0.39$) and non-advancing mode ($p^{\text{non-adv}} = 0.42$), respectively. The step size distribution is similar to the distribution acquired at 1 mM ATP (Figure 4B). The major peak of advancing forward steps is centered at 8 nm with a shoulder at 12 nm, while large non-advancing steps (12-20 nm) dominate the non-advancing mode as is the case under saturating ATP conditions. (B) Example trace segments of dynein stepping under 3 pN load at 10 μM ATP. The raw stepping data is shown in black and the steps detected by the step finding program in red (advancing mode) and blue (non-advancing mode), respectively.

Figure S10. Example stepping records of single dynein molecules under 6 pN constant rearward. The trace segments demonstrate long stretches of non-advancing stepping (trace segment a), and non-advancing stepping intermixed with single advancing steps (trace segments b, c and d; the advancing steps are indicated by the red arrowheads).

Figure S11. Statistical analyses on the combined step size data of full-length dynein
(A) Forward steps are more likely to follow a forward step at lower loads or when the last forward step is a smaller step. Probability p for taking a forward step f'' versus a backward step b'' of any size as a function of the size of the preceding forward step f' at 1, 3, 6, and 7 pN load. (B) Large forward-backward steps have a higher probability than statistically expected of being the same size. Transition probability matrix that describes the probabilities for taking different sized backward steps b following a particular sized forward step f (combined 3 pN data) (n = 5-82). The probabilities for forward steps of 12, 16 and 20 nm size to be followed by backward steps of the same size (0.46 ± 0.06, 0.45 ± 0.05 and 0.48 ± 0.06, respectively) are significantly larger than the statistically expected probabilities of 0.24 ± 0.02, 0.27 ± 0.02 and 0.15 ± 0.02 calculated from the combined histogram of backward steps in Figure 4B. (C) Large forward-backward steps are more likely to occur in clusters than short forward-backward steps at 3 pN load. Clustering probability distributions $p(n)$ of the number n of consecutive forward-backward steps of 8, 12, 16 and 20 nm at 3 pN load. A probability distribution was obtained by normalizing the histogram of measured cluster sizes by the number N of measured clusters (n = 17-34). The distributions are well fit by the exponential function $p_1 \exp[-(n-1)/n_c]$, with p_1 being the probability for observing a single or subsequent step and n_c being the characteristic cluster size. The analysis yields cluster sizes of $n_c^{12\,\mathrm{nm}} = 1.90 \pm 0.28$, $n_c^{16\,\mathrm{nm}} = 2.28 \pm 0.34$ and $n_c^{20\,\mathrm{nm}} = 2.29 \pm 0.41$. These values are significantly larger than the statistically expected sizes of $n'^{12\,\mathrm{nm}}_c = 1.23 \pm 0.01$, $n'^{16\,\mathrm{nm}}_c = 1.23 \pm 0.01$ and $n'^{20\,\mathrm{nm}}_c = 1.18 \pm 0.01$, with $n'_c = 1 - \ln^{-1} p'$ being the expected characteristic cluster size and p' being the expected probability (assuming no dependency between subsequent steps) to observe a single or a subsequent forward-backward step of size d (calculated from the combined step size histogram in Figure 4B); the expected probability to observe n clustered steps of the same size is given by $(p')^n$ and the clustering probability distribution function is expressed by $p' \exp[-(n-1)/n'_c]$. In contrast to the clustering of the large (12-20 nm) steps, clustered 8 nm forward-backward steps did not occur more often than statistically expected. The estimated probability of 0.0243 ± 0.0022 (which corresponds to a cluster size of $n'^{8\,\mathrm{nm}}_c = 1 - 1/\ln(0.0243) = 1.27$, see blue curve in panel C) for an 8 nm forward-backward step to occur suggests that, on average, 0.9 of 35 observed forward-backward steps will be followed by a subsequent step of the same size. In agreement with this estimation, only 1 of 35 detected 8 nm forward-backward steps was followed by a forward-backward step of the same size (panel C, blue data points). It should be noted that the measured cluster sizes (panels C and D) are an underestimate of the actual cluster sizes due to the underlying method of assigning steps to a step size d (8, 12, 16 or 20 nm). A measured forward-backward step was assigned to the step size d if both the measured forward step size d'_f and the measured subsequent backward step size d'_b met the criterion $d - 2\,\mathrm{nm} \le d'_f, d'_b < d + 1.9\,\mathrm{nm}$ (same criterion used for all step size analyses presented in this figure). While this criterion prevents double step size assignments, it leads to some false assignments. The major effect of false assignments is caused by steps falling outside of the defined range of step size d (due to the width of the step size distributions, the SD is estimated to be 1.6 nm) even though they were drawn from a distribution of mean d. This effect leads to significantly smaller apparent cluster sizes. In fact, approximately one out of five steps (forward or backward) will fall outside of the defined range and not be identified as a step of size d assuming a distribution with mean d and SD of 1.6 nm, which explains the absence of measured cluster sizes of $n > 4$ in most of the

distributions shown in panels C and D. (D) Large forward-backward steps are more likely to occur in clusters than short forward-backward steps at 6 pN load. Probability distributions of measured cluster sizes of 8, 12 and 16 nm forward-backward steps of the same size at 6 pN load. Fit results: $n_c^{8\,\mathrm{nm}} = 1.38 \pm 0.12$, $n_c^{12\,\mathrm{nm}} = 2.16 \pm 0.25$ and $n_c^{16\,\mathrm{nm}} = 1.89 \pm 0.36$ (n = 13-37). The statistically expected cluster sizes are $n'^{8\,\mathrm{nm}}_c = 1.27 \pm 0.01$, $n'^{12\,\mathrm{nm}}_c = 1.3 \pm 0.01$ and $n'^{16\,\mathrm{nm}}_c = 1.19 \pm 0.004$. (A-D) All error estimates given in this figure were calculated as the SD of fit parameters (or probability values) derived from 200 bootstrap samples of the underlying data sets.

Figure S12. Cumulative probability functions of dwell time distributions for non-advancing forward and non-advancing backward steps as a function of load and ATP concentration. The distributions are well fit by the cumulative probability function $1 - \exp(-kt)$ derived for a single exponential dwell time distribution (the given error estimates were calculated as the SD of the fit rates derived from 200 bootstrap trials) (n = 121-419). These fits were used to derive the rate constants reported in Figure 5B. At 10 μM ATP (a value close to K_m, see legend to Figure S9), we might expect to find the cumulative frequency plots of the dwell time distributions of forward steps best fit to a kinetic scheme with two rate-limiting transitions reflecting sequential processes of ATP binding followed by a first-order transition that limited the cycle at saturating ATP. However, the cumulative probability function of a convolution of two exponentials (Gebhardt et al., 2006) did not significantly improve the fits at 10 μM ATP according to the Bayesian information criterium (Schwarz, 1978). The reason for this is not clear, but it could reflect distinct kinetic pathways operating at high and low ATP, perhaps reflecting site occupancy of the four ATP binding sites in dynein. Further work will be needed to explore this possibility. However, the data clearly shows an effect of lowering ATP on k_f (rate constant for forward stepping) but no effect on k_b, thus identifying the ATP-dependent step in the repetitive forward-backward stepping cycle observed when dynein is placed under load.

Figure S13. GST-Dyn1$_{331\mathrm{kDa}}$ stepping at 3 pN constant rearward load showing advancing and non-advancing stepping behaviors. (A) Bead position (black trace) and trap position (green trace) as a function of time. Bead movement was analyzed in a detection area of ±200 nm (indicated by the dashed line) within which the motor experiences a constant load from the feedback-controlled optical trap (trap stiffness: k = 0.054 pN/nm). (B) Example trace segments with detected steps. The segments correspond to the parts of the displacement trace shown in A and indicated by the black bars. The raw data is shown in black and the steps detected by the step finding program in red (advancing mode) and blue (non-advancing mode), respectively. Additional stepping data is shown in Figure 6 of the paper.

Figure S14. GST-Dyn1$_{314\mathrm{kDa}}$ stepping at 3 pN constant rearward load showing predominantly advancing stepping behavior and force-induced microtubule plus- and minus-end-directed stepping in the absence of ATP binding and hydrolysis. (A) Bead position (black trace) and trap position (green trace) as a function of time. Bead movement was analyzed in a detection area of ±200 nm (indicated by the dashed line) within which the motor experiences a constant load from the feedback-controlled optical trap (trap stiffness: k = 0.054 pN/nm). (B) Example trace segments with detected steps. The segments correspond to the parts of the displacement trace shown in A and indicated by the black bars. Additional stepping data is

shown in Figure 6 of the paper. (C) Example record of forced-backward stepping at 7 pN rearward load in the absence of ATP (trap stiffness: $k = 0.061$pN/nm). The trace segments marked by a and b correspond to the parts of the displacement trace shown above. (D) Force-induced ATP-independent microtubule minus-end-directed stepping under –3 pN forward load (trap stiffness: $k = 0.061$pN/nm). The trace segments marked by a and b correspond to the parts of the displacement trace shown above. Under an assisting load of -3 pN, ~90% of the dynein-coated beads (30 out of 34) that bound to a microtubule exhibited continuous movement within a ~10 s window of applied load with an average velocity of 15.1 ± 4.1 nm/s. In contrast, a much higher rearward force of 10 pN was needed to induce efficient (~90%; 15 out of 17 beads) stepping toward the microtubule plus-end (-11.8 ± 3.9 nm/s) within a similar period of applied force. At 7 pN (the stall force), fewer beads (27 out of 43) moved in a similar period of applied force. (B-D) Bead positions (raw data) are drawn in black and the steps detected by the step finding program in red (advancing mode) and blue (non-advancing mode), respectively.

Figure S15. GST-α2-Dyn1$_{314kDa}$ stepping at 3 pN constant rearward load showing advancing and non-advancing stepping behaviors. The raw data is shown in black and the steps detected by the step finding program in red (advancing mode) and blue (non-advancing mode), respectively. Additional stepping data is shown in Figure 6 of the paper.

Figure S16. Possible walking sequences explaining 4, 8, 12 and 24 nm steps. (A) Illustration of the alternating shuffling, hand-over-hand-like mechanism giving rise to 8, 12 or 24 nm center-of-mass steps. Step sizes of 16 and 20 nm are correspondingly explained by other variations in the spacing between the two heads before and after the ATP-induced step. (B) Consecutive forward steps of ~4 nm can be most easily explained by an inchworm-like mechanism. Here, both heads retain there trailing and leading roles (in the example shown, the dark grey head occupies the leading role) (see main text for further information). (C) An alternate mechanism for inchworm-like stepping. The two heads are in the "extended" state in which the heads are separated by more than 8 nm along a the microtubule axis; the trailing head can move forward to the next unoccupied binding site (light colored) without passing the leading head (dark grey), resulting in a center-of-mass displacement of ~4 nm toward the minus-end of the microtubule.

Figure S17. Ratio of forward to backward steps in the advancing mode of full-length dynein as a function of constant rearward load at 1 mM ATP. The data is calculated from the step size histograms shown in Figure 4 (red histogram bars). The dashed line represents the fit to the equation $R_0 \exp(-Fd/k_BT)$, where $R_0 = \exp[(E_b - E_F)/k_BT]$ with E_f and E_b being the heights of the energy barrier maxima in forward and backward direction at zero load and d being the difference of the characteristic distances (Nishiyama et al., 2002). Fit result: $R_0 = 3.79$ and $d = 0.81$nm. The energy difference between the barrier heights in forward and backward direction is shown on the right and was $\ln(R_0)k_BT = 1.33k_BT$ at zero load.

Figure S18. Step size analysis of simulated stepping traces
(A) Histogram of step sizes (n = 451) detected in simulated stepping traces with 8 nm forward and backward steps under 1 pN load and 1 mM ATP. (B) Histogram of step sizes (n = 705) detected in simulated stepping traces with different fractions of hidden forward and backward steps of 4, 8, 12 and 16 nm. The histogram of forward steps can be described by multiple Gaussian functions with a uniform distribution width (SD = 1.3 nm) with peaks at 5.1 nm

(15.2%), 8 nm (45.2%), 12 nm (21.5%), 16 nm (15.7%) and 20 nm (2.5%) (black curve). (C) Example trace segments of simulated stepping traces with a mixture of different sized steps (4, 8, 12 and 16 nm). The generated optical trapping-based data is shown in black, the simulated steps prior to noise addition in green and the steps detected by the step finding program in red (the red and green numbers indicate the detected and simulated step sizes). Occasionally the algorithm fitted noise (marked by the black arrowheads) due to an "overfitting" of the data; these "steps" were not taken into account.

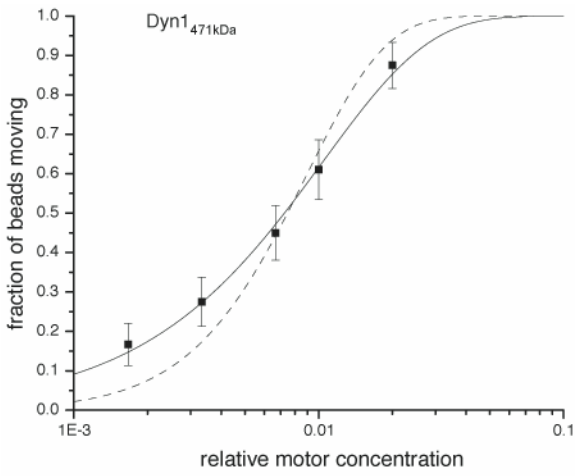
Dyn1471kDa
fraction of beads moving
relative motor concentration
1.0
0.9
0.8
0.7
0.6
0.5
0.4
0.3
0.2
0.1
0.0
1E-3
0.01
0.1

Figure S1

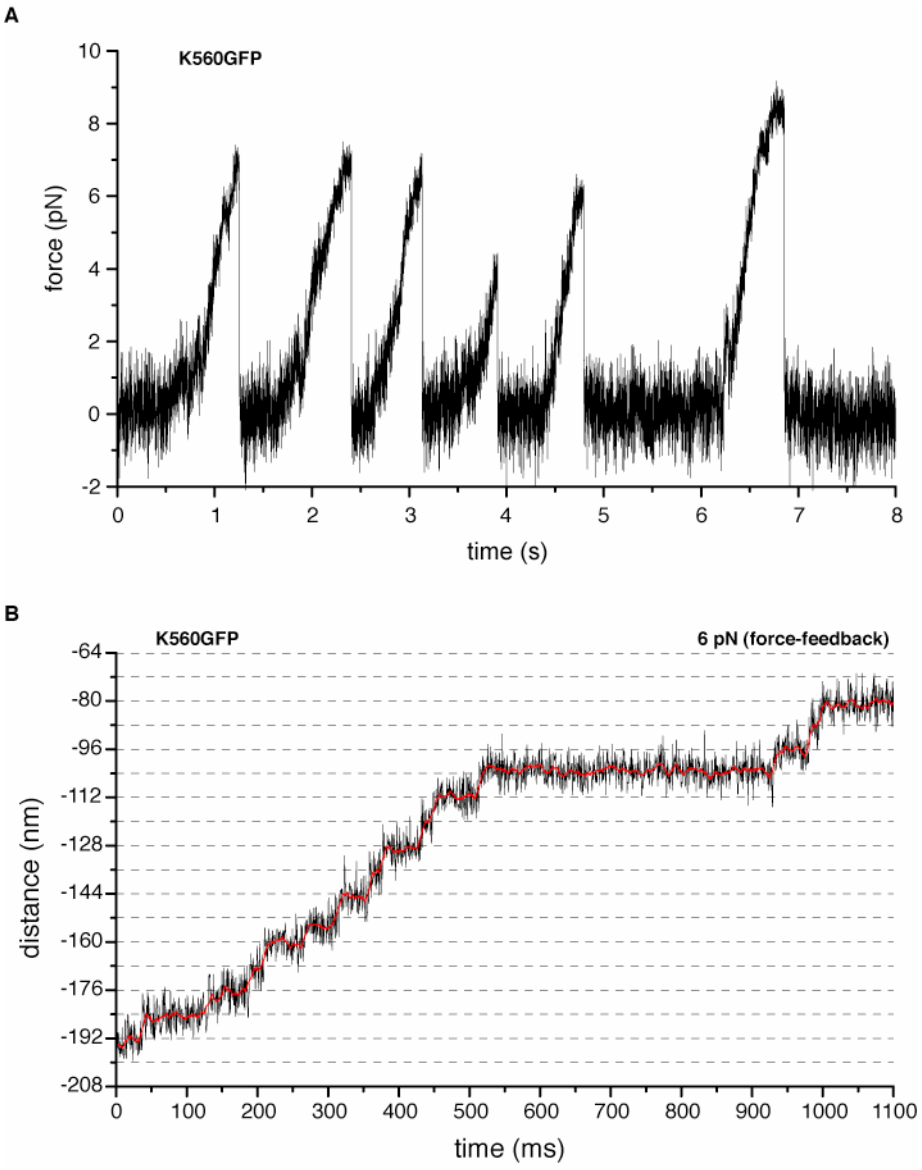
A
K560GFP
force (pN)
time (s)
B
K560GFP
6 pN (force-feedback)
distance (nm)
time (ms)

Figure S2

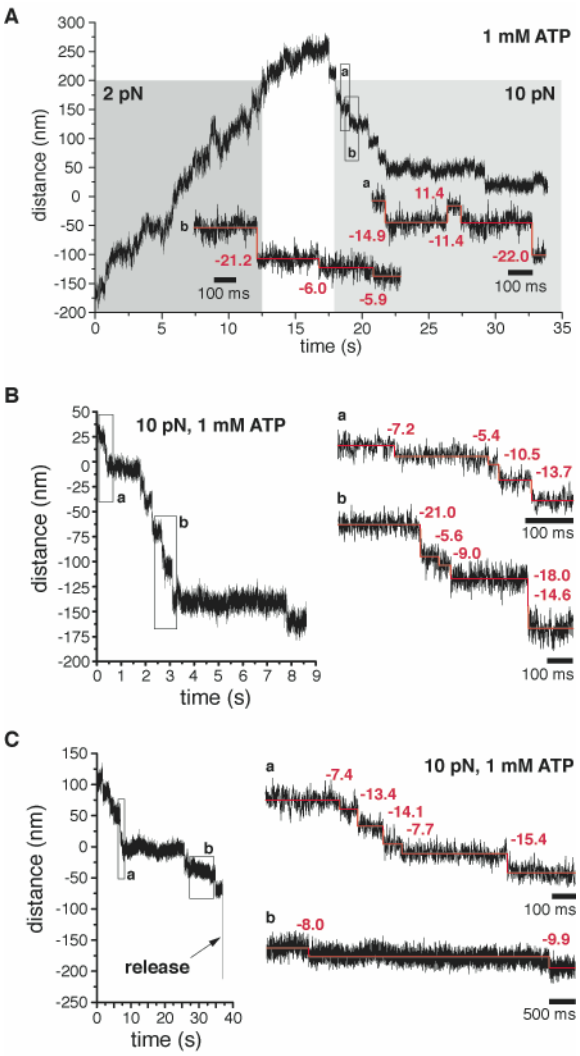
A
1 mM ATP
2 pN
10 pN
distance (nm)
time (s)
100 ms
-21.2
-6.0
-5.9
11.4
-14.9
-11.4
-22.0
B
10 pN, 1 mM ATP
-7.2
-5.4
-10.5
-13.7
-21.0
-5.6
-9.0
-18.0
-14.6
C
release
-7.4
-13.4
-14.1
-7.7
-15.4
-8.0
-9.9
500 ms

Figure S3

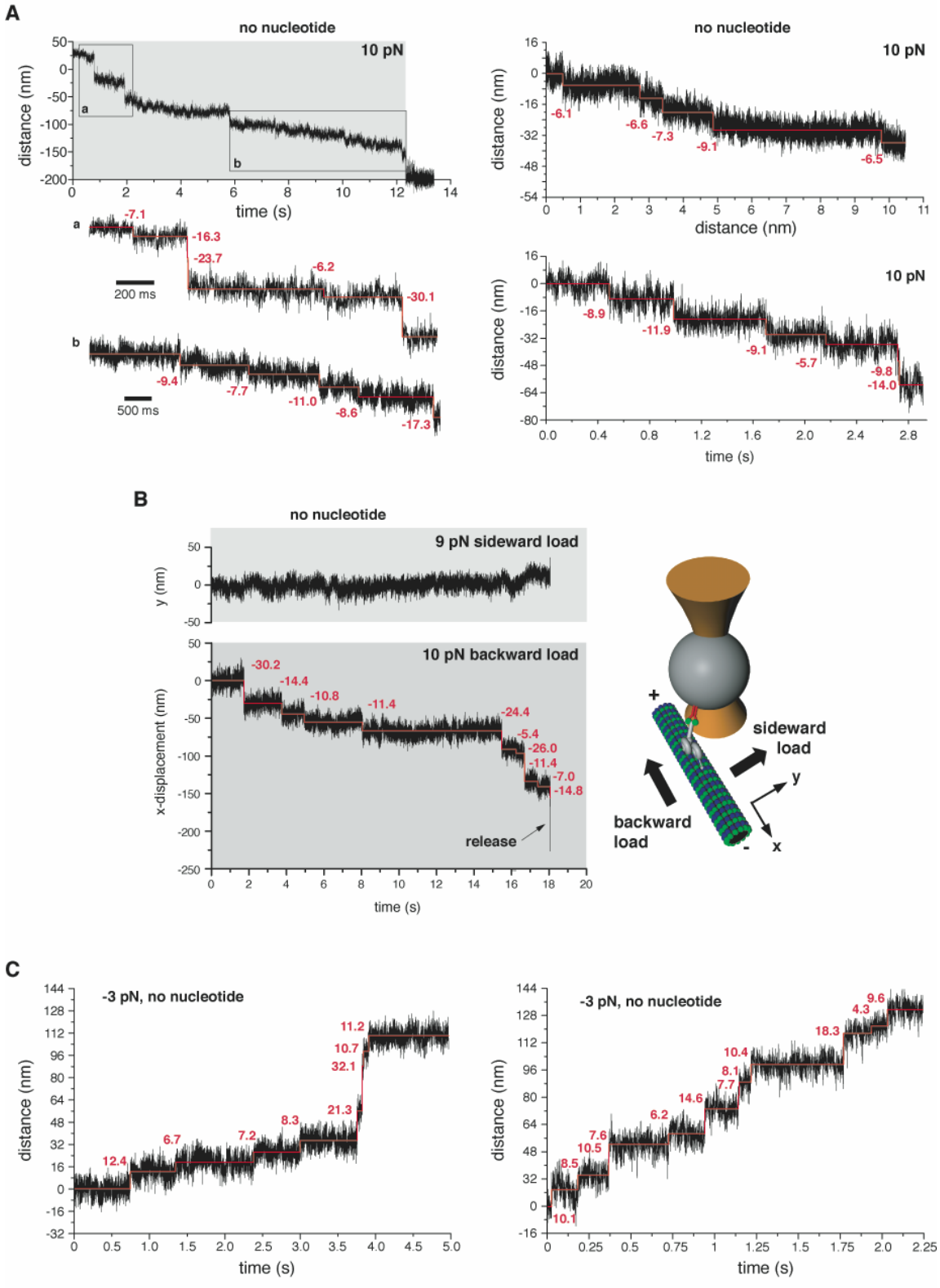
A
no nucleotide
10 pN
distance (nm)
time (s)
a
b
-7.1
-16.3
-23.7
-6.2
-30.1
200 ms
-9.4
-7.7
-11.0
-8.6
-17.3
500 ms
no nucleotide
10 pN
-6.1
-6.6
-7.3
-9.1
-6.5
distance (nm)
10 pN
-8.9
-11.9
-9.1
-5.7
-9.8
-14.0
time (s)
B
no nucleotide
9 pN sideward load
y (nm)
10 pN backward load
x-displacement (nm)
-30.2
-14.4
-10.8
-11.4
-24.4
-5.4
-26.0
-11.4
-7.0
-14.8
release
time (s)
+
-
sideward load
backward load
y
x
C
-3 pN, no nucleotide
distance (nm)
12.4
6.7
7.2
8.3
21.3
32.1
10.7
11.2
time (s)
-3 pN, no nucleotide
10.1
8.5
10.5
7.6
6.2
14.6
7.7
8.1
10.4
18.3
4.3
9.6
time (s)

Figure S4

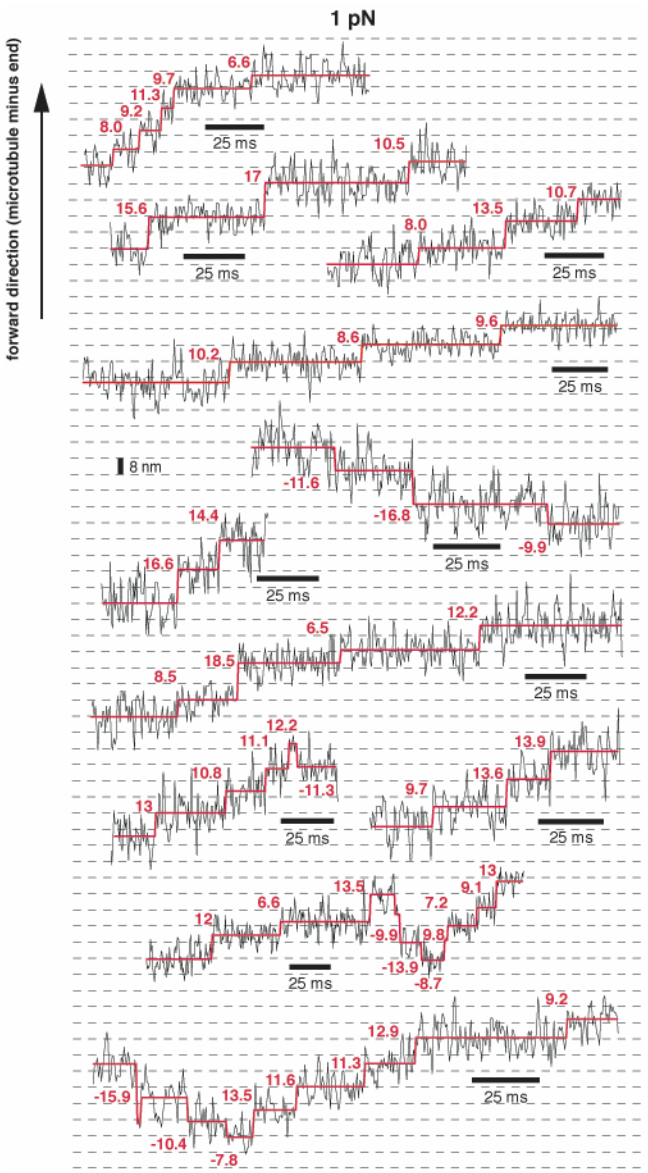
1 pN
forward direction (microtubule minus end)
8 nm
25 ms
6.6
9.7
11.3
9.2
8.0
10.5
17
15.6
13.5
10.7
8.0
9.6
8.6
10.2
-11.6
-16.8
-9.9
14.4
16.6
12.2
6.5
18.5
8.5
12.2
11.1
13.9
10.8
-11.3
9.7
13.6
13
13
13.5
9.1
7.2
6.6
12
-9.9
9.8
-13.9
-8.7
9.2
12.9
11.3
11.6
13.5
-15.9
-10.4
-7.8

Figure S5

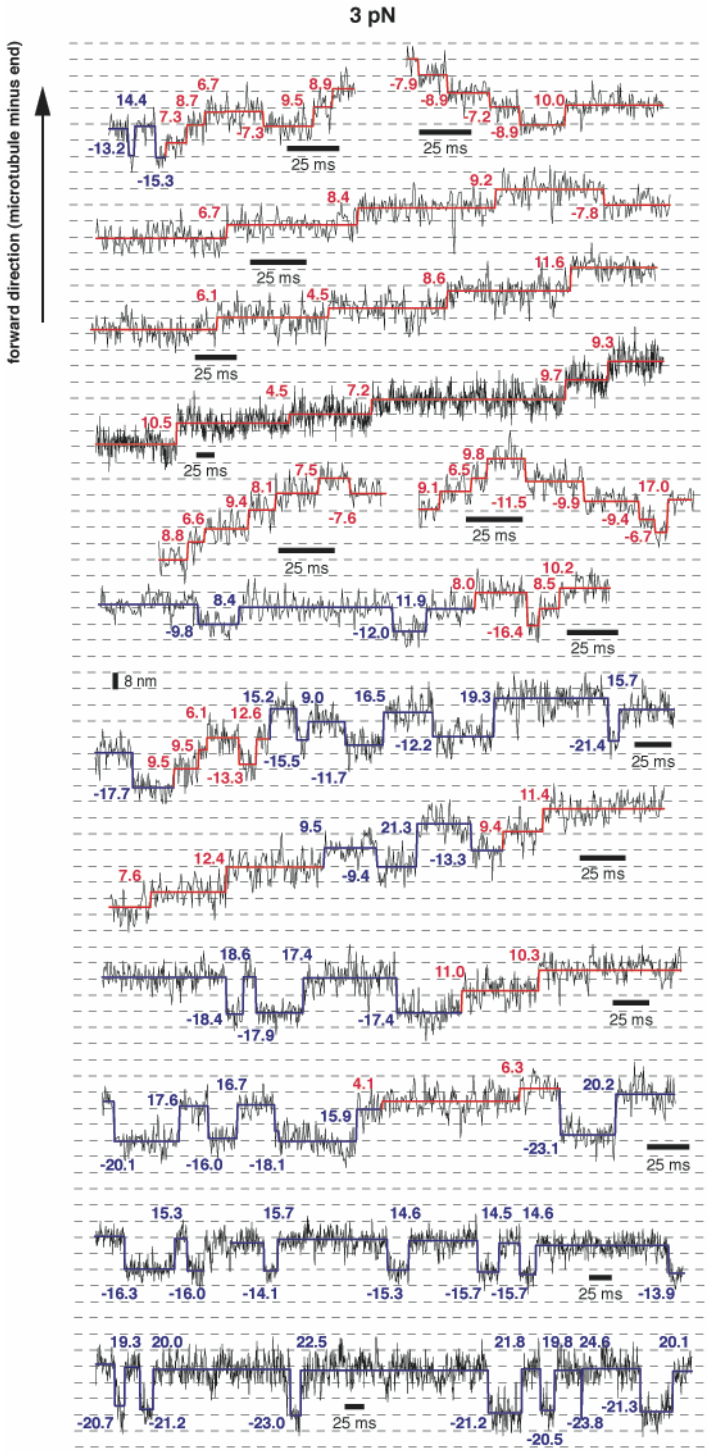

Figure S6

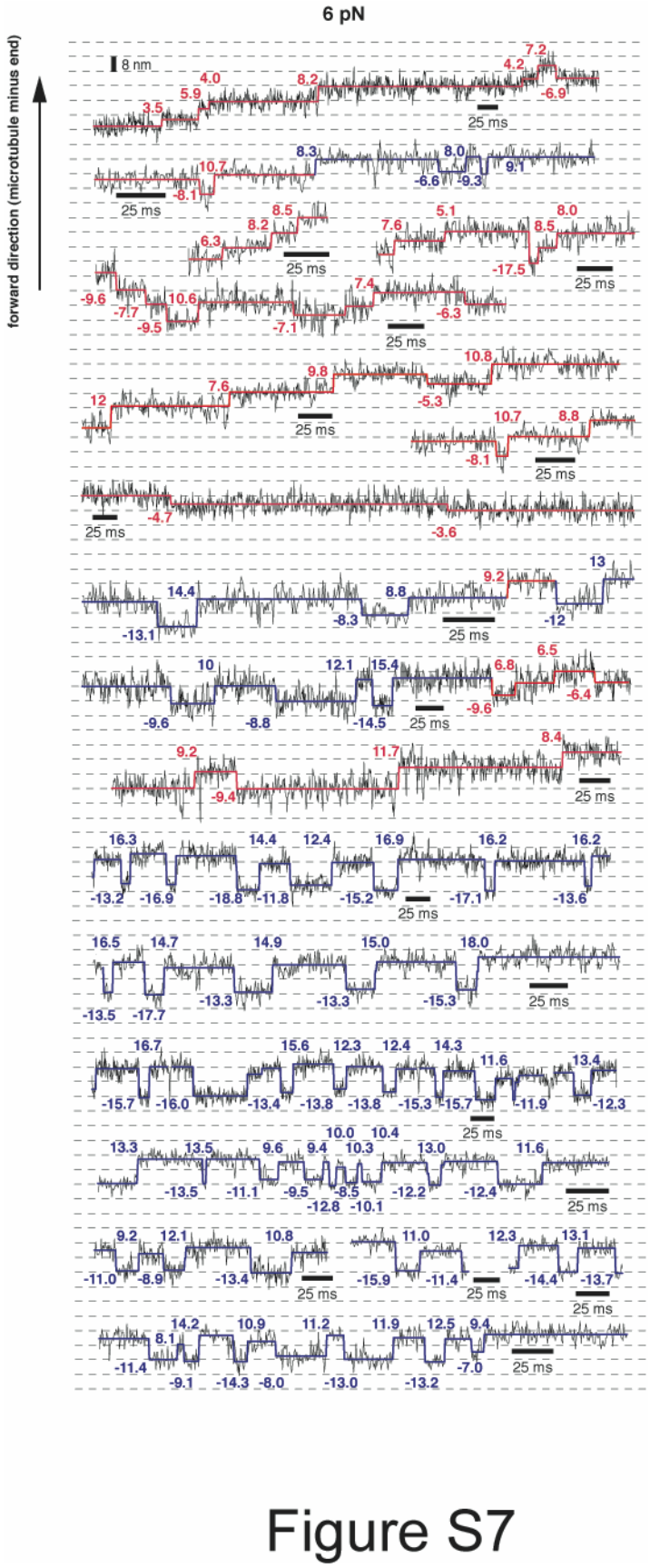

Figure S7

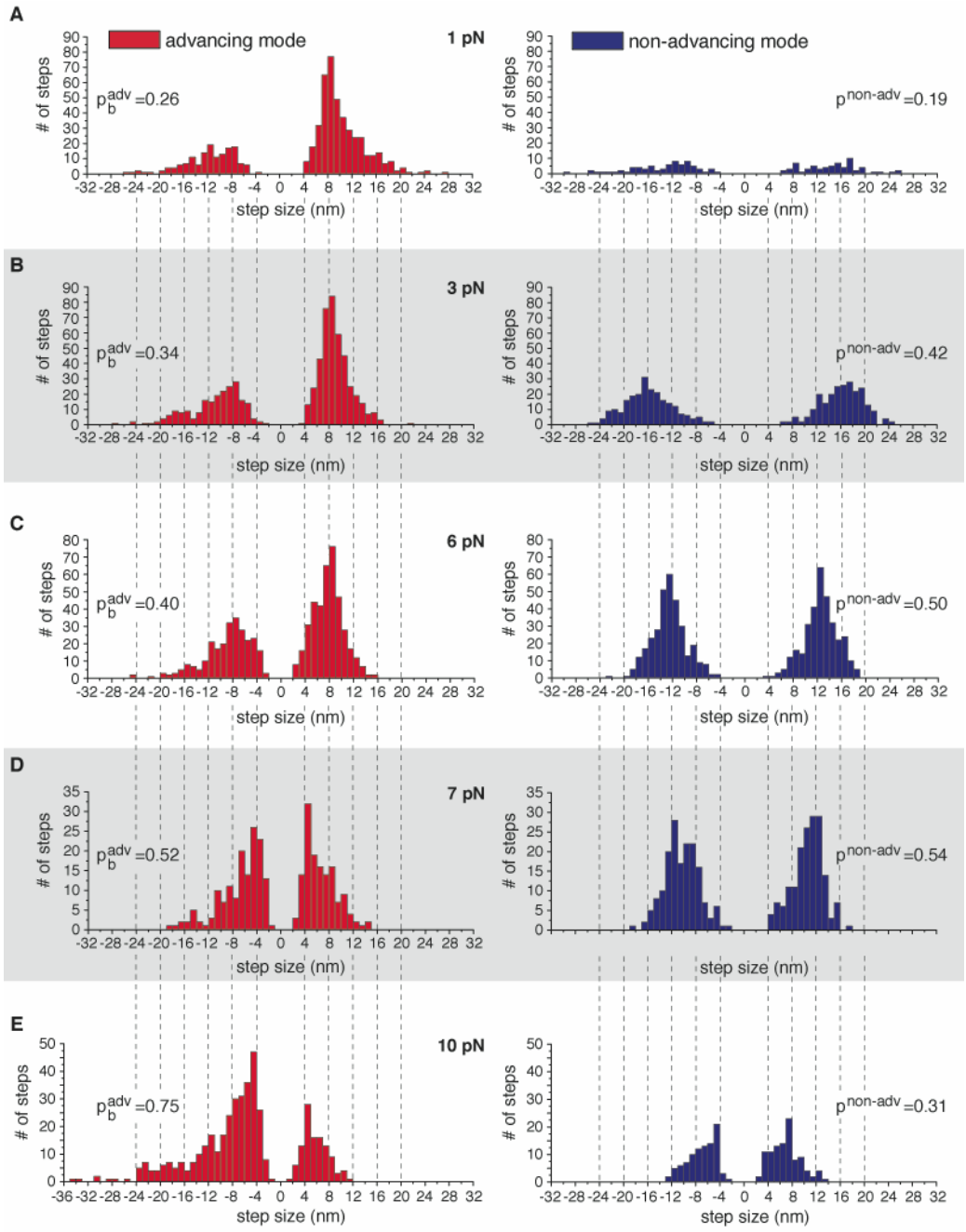
A
advancing mode
1 pN
non-advancing mode
p_b^{adv}=0.26
$p^{non-adv}$=0.19
B
3 pN
p_b^{adv}=0.34
$p^{non-adv}$=0.42
C
6 pN
p_b^{adv}=0.40
$p^{non-adv}$=0.50
D
7 pN
p_b^{adv}=0.52
$p^{non-adv}$=0.54
E
10 pN
p_b^{adv}=0.75
$p^{non-adv}$=0.31
# of steps
step size (nm)

Figure S8

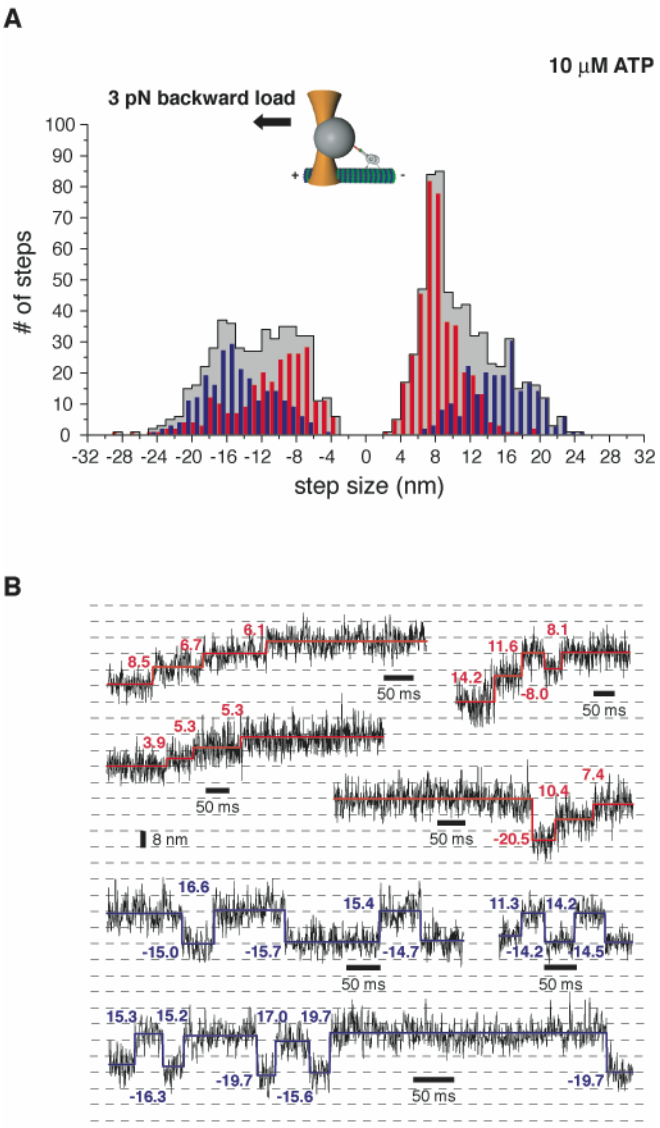

Figure S9

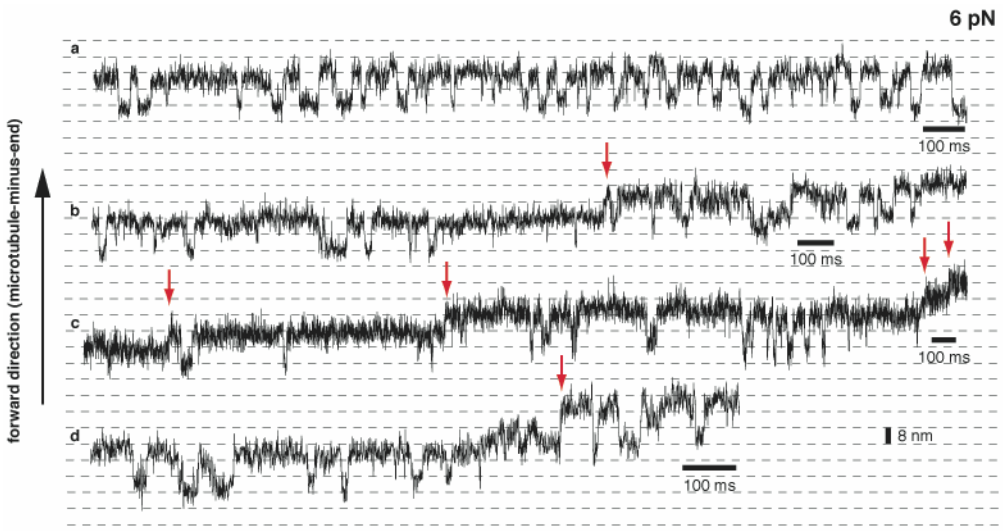
6 pN
a
b
c
d
100 ms
100 ms
100 ms
100 ms
8 nm
forward direction (microtubule-minus-end)

Figure S10

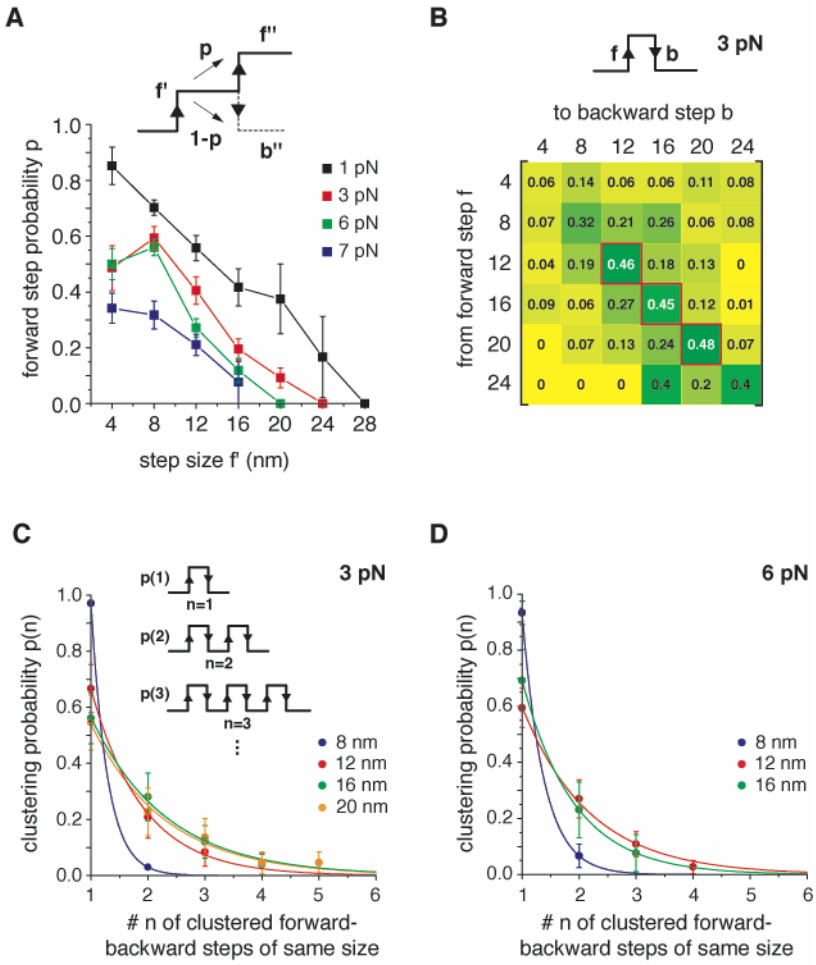
A
p
f''
f'
1-p
b''
1.0
0.8
0.6
0.4
0.2
0.0
forward step probability p
4 8 12 16 20 24 28
step size f' (nm)
1 pN
3 pN
6 pN
7 pN
B
f
b
3 pN
to backward step b
4 8 12 16 20 24
from forward step f
4 0.06 0.14 0.06 0.06 0.11 0.08
8 0.07 0.32 0.21 0.26 0.06 0.08
12 0.04 0.19 0.46 0.18 0.13 0
16 0.09 0.06 0.27 0.45 0.12 0.01
20 0 0.07 0.13 0.24 0.48 0.07
24 0 0 0 0.4 0.2 0.4
C
3 pN
p(1)
n=1
p(2)
n=2
p(3)
n=3
clustering probability p(n)
1.0
0.8
0.6
0.4
0.2
0.0
1 2 3 4 5 6
n of clustered forward-backward steps of same size
8 nm
12 nm
16 nm
20 nm
D
6 pN
clustering probability p(n)
1.0
0.8
0.6
0.4
0.2
0.0
1 2 3 4 5 6
n of clustered forward-backward steps of same size
8 nm
12 nm
16 nm

Figure S11

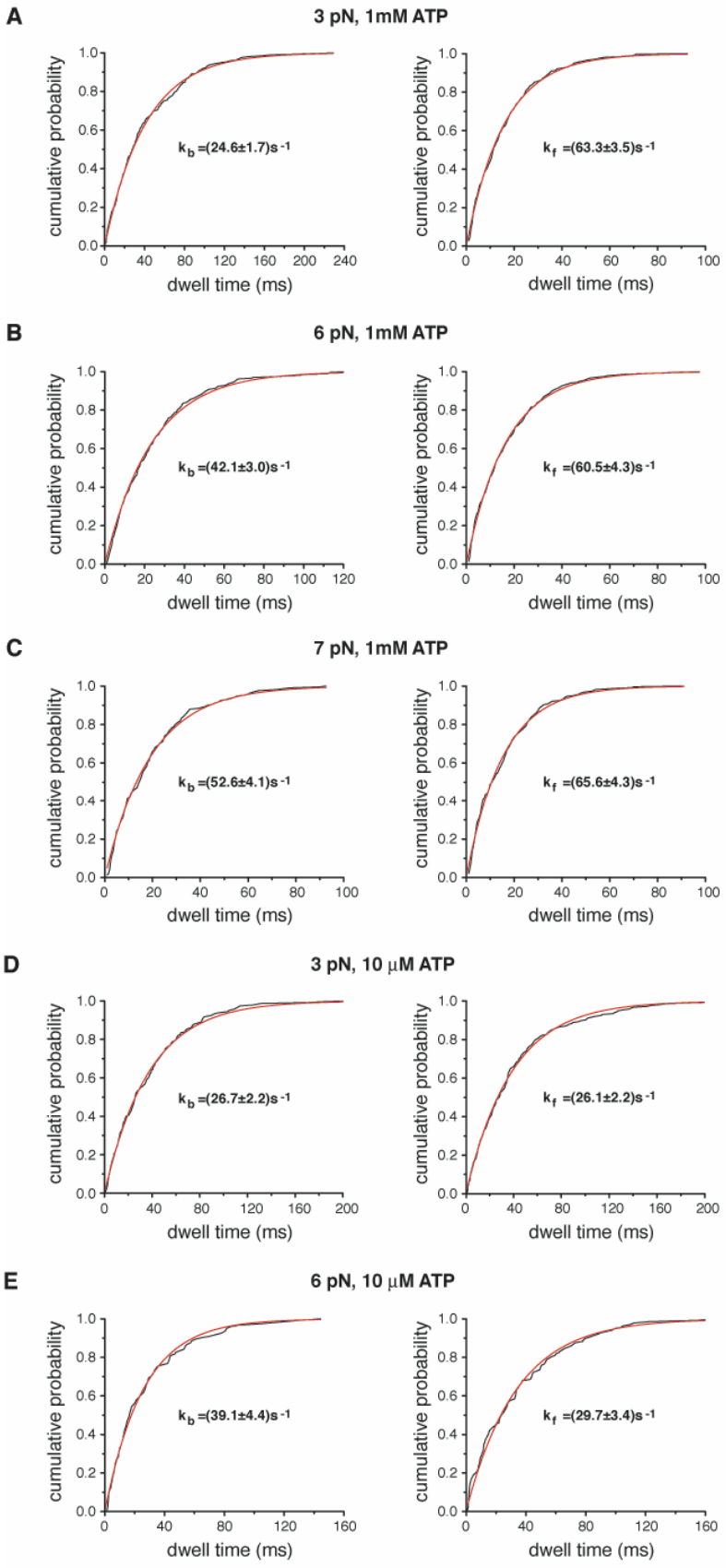
A
3 pN, 1mM ATP
cumulative probability
dwell time (ms)
k_b =(24.6±1.7)s^{-1}
k_f =(63.3±3.5)s^{-1}
B
6 pN, 1mM ATP
k_b =(42.1±3.0)s^{-1}
k_f =(60.5±4.3)s^{-1}
C
7 pN, 1mM ATP
k_b =(52.6±4.1)s^{-1}
k_f =(65.6±4.3)s^{-1}
D
3 pN, 10 μM ATP
k_b =(26.7±2.2)s^{-1}
k_f =(26.1±2.2)s^{-1}
E
6 pN, 10 μM ATP
k_b =(39.1±4.4)s^{-1}
k_f =(29.7±3.4)s^{-1}

Figure S12

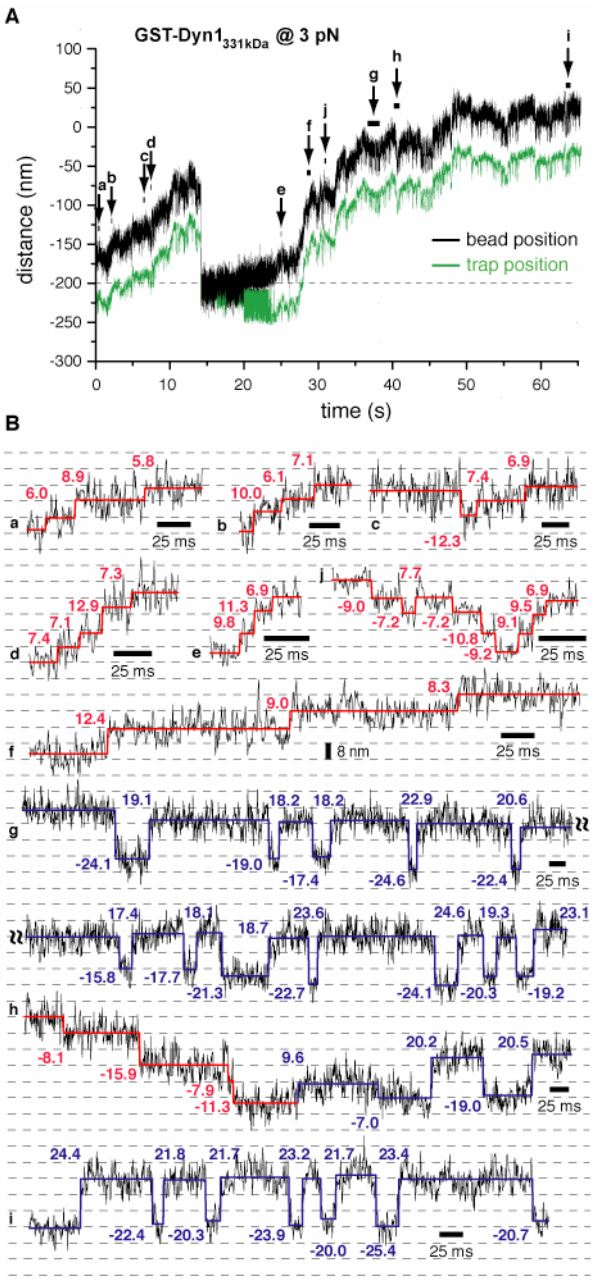
A
GST-Dyn1331kDa @ 3 pN
distance (nm)
time (s)
bead position
trap position
B
25 ms
8 nm

Figure S13

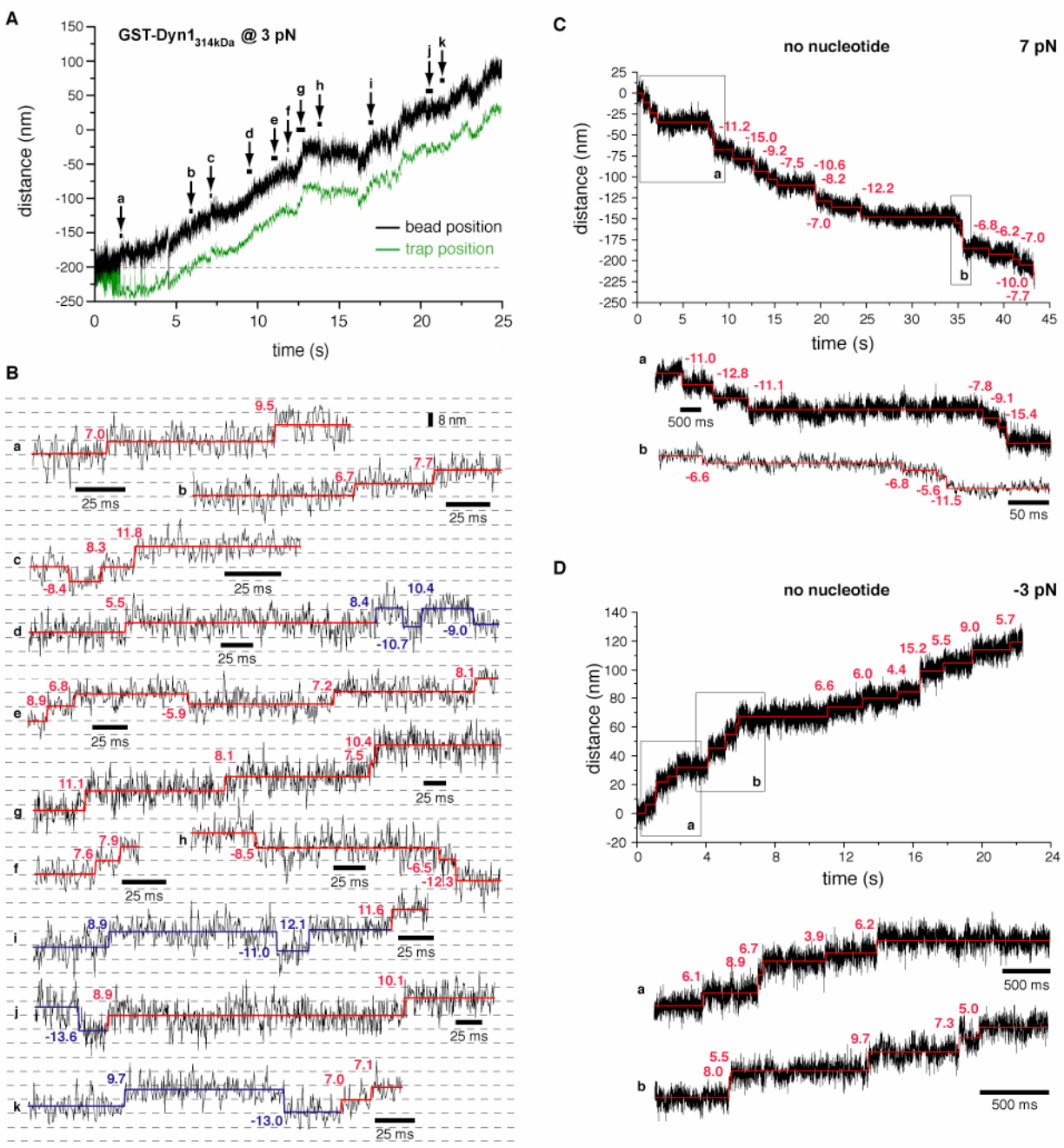
A
GST-Dyn1314kDa @ 3 pN
distance (nm)
time (s)
bead position
trap position
B
8 nm
25 ms
C
no nucleotide
7 pN
distance (nm)
time (s)
500 ms
50 ms
D
no nucleotide
-3 pN
distance (nm)
time (s)
500 ms

Figure S14

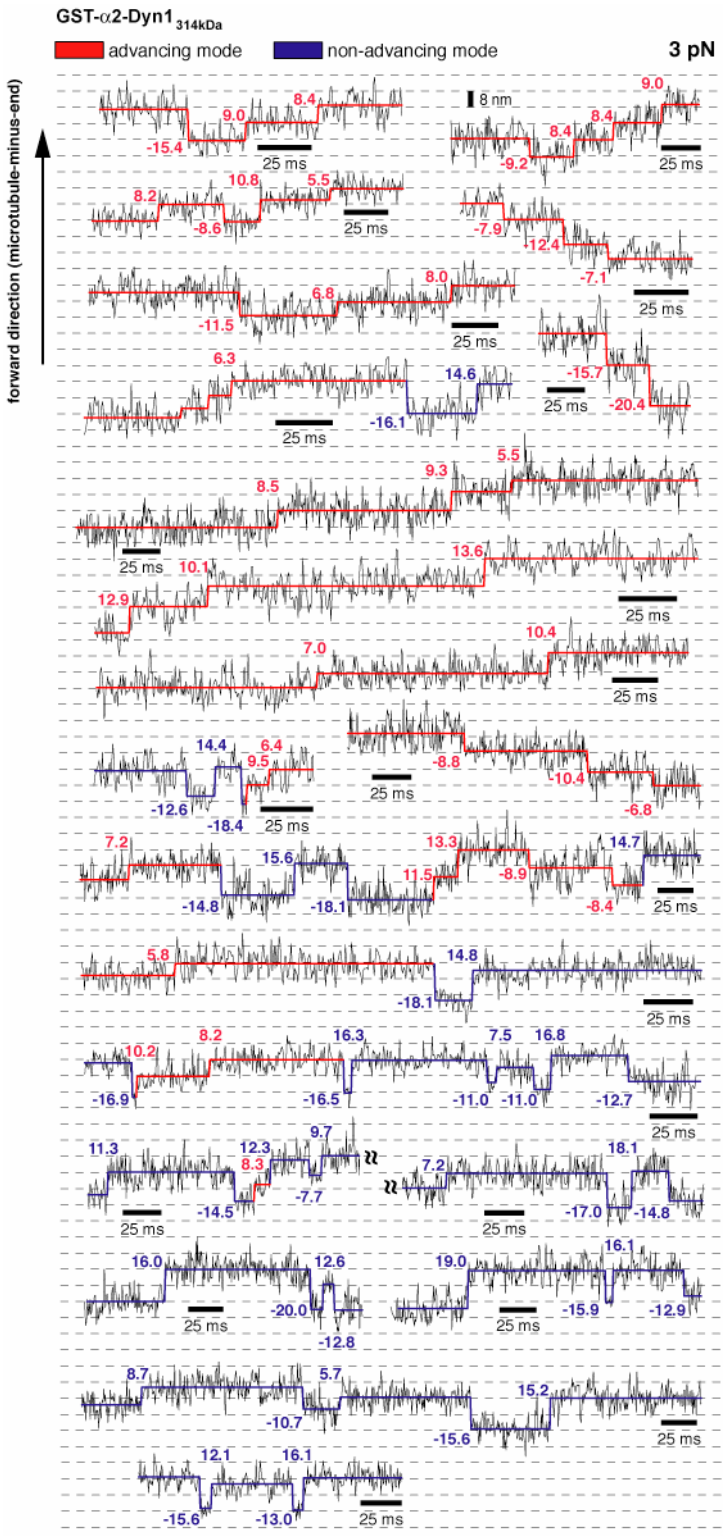
GST-α2-Dyn1 314kDa
advancing mode
non-advancing mode
3 pN
forward direction (microtubule-minus-end)
8 nm
25 ms

Figure S15

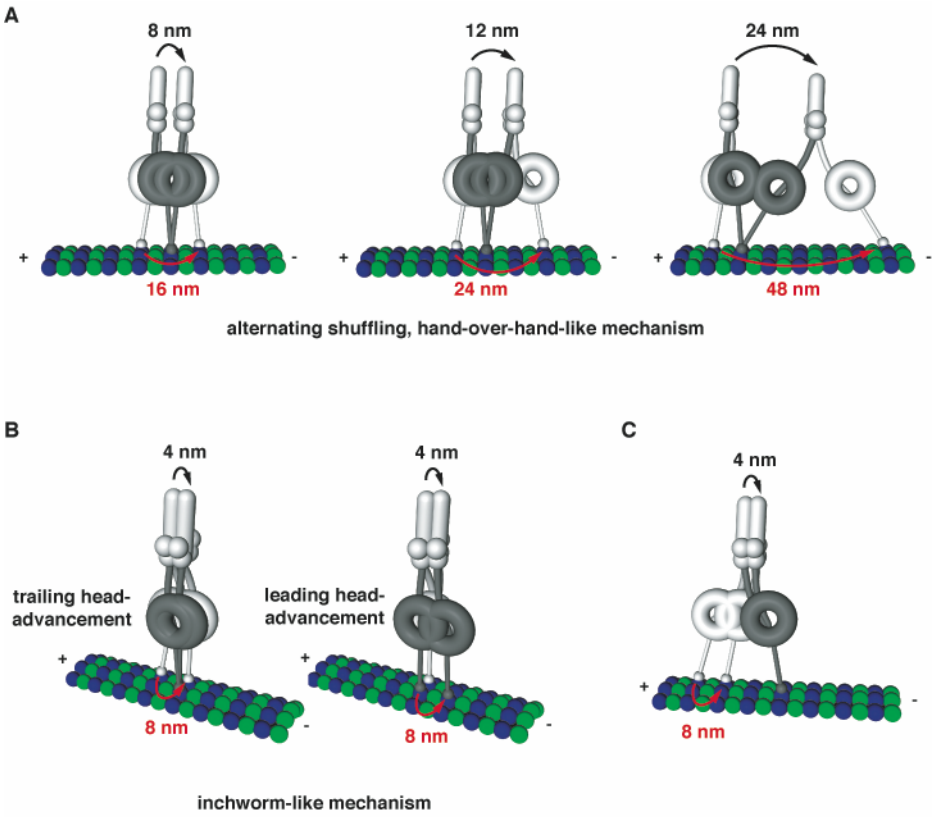
A
8 nm
12 nm
24 nm
+
-
16 nm
24 nm
48 nm
alternating shuffling, hand-over-hand-like mechanism
B
4 nm
4 nm
trailing head-advancement
leading head-advancement
8 nm
8 nm
C
4 nm
8 nm
inchworm-like mechanism

Figure S16

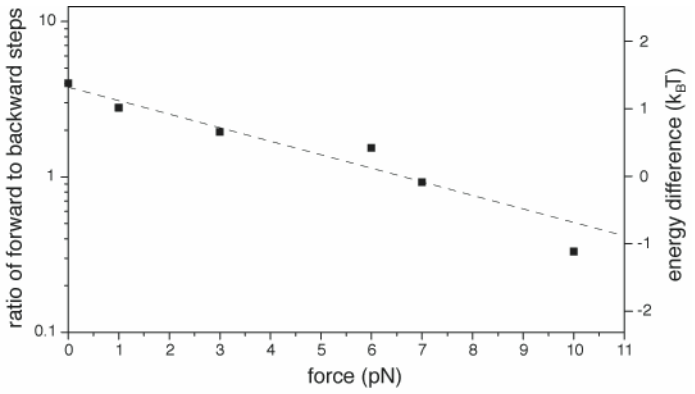
ratio of forward to backward steps
energy difference (k_BT)
force (pN)
10
1
0.1
2
1
0
-1
-2
0
1
2
3
4
5
6
7
8
9
10
11

Figure S17

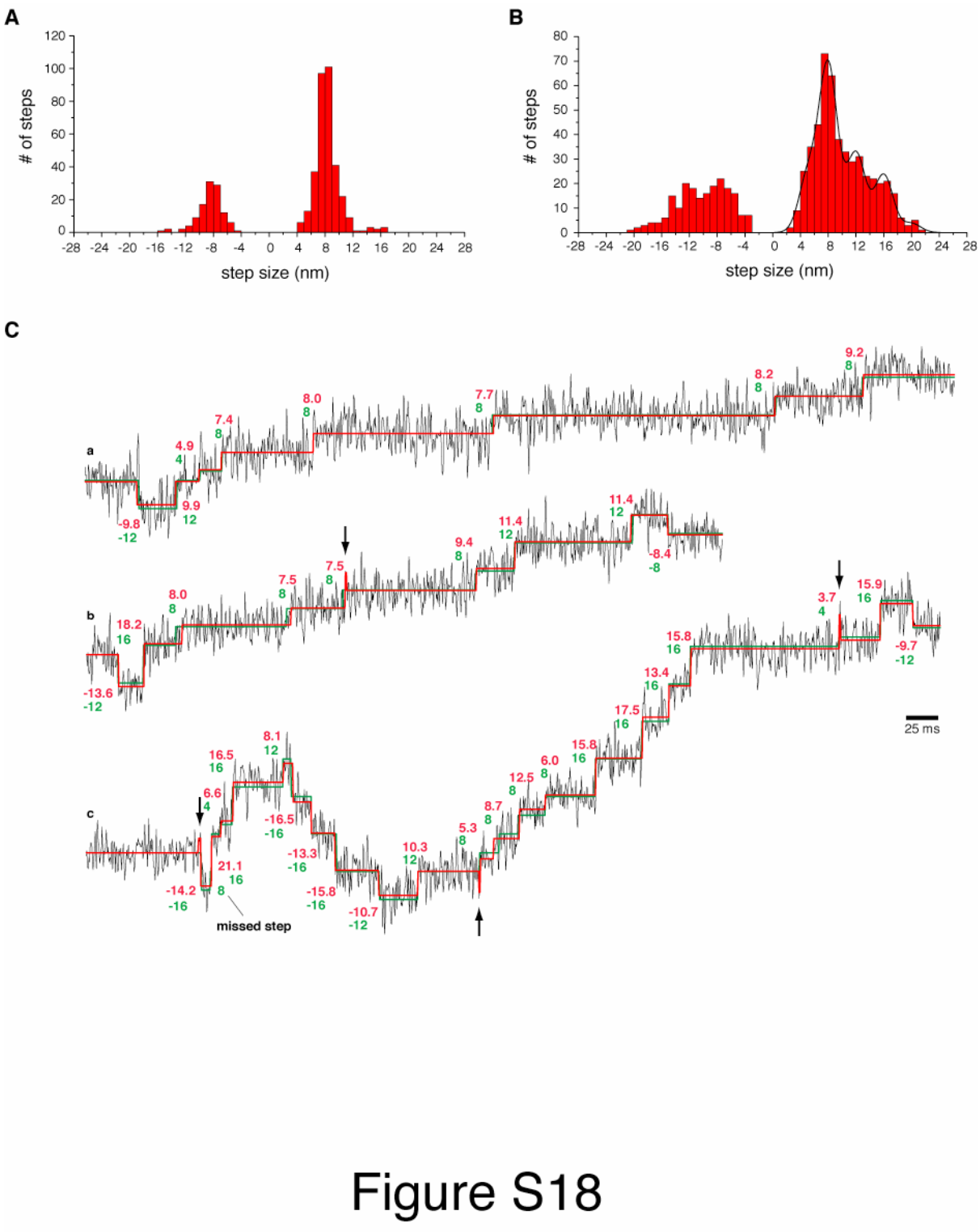
A
# of steps
step size (nm)
B
# of steps
step size (nm)
C
a
b
c
missed step
25 ms

Figure S18